Pro gradu -tutkielma
Meteorologia

A multi-instrument approach for studying complex patterns of turbulent mixing

Pyry Pentikäinen
2017

Ohjaajat: Ewan O'Connor
Antti Manninen
Tarkastajat: Tuukka Petäjä
Dmitri Moisseev

HELSINGIN YLIOPISTO
FYSIIKAN LAITOS

PL 64 (Gustaf Hällströmin katu 2)
00014 Helsingin yliopisto

HELSINGIN YLIOPISTO — HELSINGFORS UNIVERSITET — UNIVERSITY OF HELSINKI

Tiedekunta/Osasto — Fakultet/Sektion — Faculty	Laitos — Institution — Department
Faculty of Science	Department of Physics

Tekijä — Författare — Author
Pyry Pentikäinen

Työn nimi — Arbetets titel — Title

A multi-instrument approach for studying complex patterns of turbulent mixing

Oppiaine — Läroämne — Subject
Meteorology

Työn laji — Arbetets art — Level	Aika — Datum — Month and year	Sivumäärä — Sidoantal — Number of pages
Pro Gradu	May 2017	53

Tiivistelmä — Referat — Abstract

Turbulent mixing in the atmospheric boundary layer above the Hyytiälä forestry field station in southern Finland was studied with a combination of Doppler lidar and in-situ measurements on a 125 m tall mast. The intensity of turbulent mixing was derived from measurements of the vertical and horizontal wind speeds. Other meteorological data was included in the analysis to aid in the interpretation process. The methods applied to the data performed robustly under standard weather conditions, and thus can be used with high confidence to study more complex patterns of turbulent mixing. This includes two case studies of turbulent mixing under complex circumstances, one of which strongly implied a causal relationship between sudden changes in heat fluxes and the initiation of a nocturnal jet. The turbulent data from Doppler lidar Vertical Azimuth Display scans were separated into directional components to study the spatial variability of turbulent mixing. No significant spatial variability was observed during the daytime when strong turbulence consisting of large–scale turbulent eddies encompassing the whole boundary layer dominate. However, significant spatial differences were sometimes seen in the growth of the mixing layer during the morning, and stark spatial variability in turbulent mixing was detected on several summer nights. No single mechanism was conclusively shown to be responsible for the observed distribution of turbulence, but the night–time variability seemed to be connected to the presence of nocturnal jets. The area of the most intense nocturnal mixing is located in the vicinity of the nearby Station for Measuring Ecosystem - Atmosphere Relations II where comprehensive aerosol and canopy exchange research is performed. The observed nocturnal mixing may have implications for the conclusions resulting from the measurements performed at the station. The thermodynamic stability of the near–surface boundary layer was investigated using scaled potential temperature profiles measured at various altitudes on the 125 m measurement mast. There was good agreement with Doppler lidar observations, but due to calibration issues in the thermometers on the mast, quantitative results lack accuracy even after corrections were applied.

Avainsanat — Nyckelord — Keywords
Turbulence, mixing layer, boundary layer, Doppler lidar, stability, nocturnal jet

Säilytyspaikka — Förvaringsställe — Where deposited

Muita tietoja — övriga uppgifter — Additional information

Contents

1 Introduction

Understanding the behaviour of mixing processes in the atmospheric boundary layer (BL) is important, because they are directly responsible for the dilution of pollution released at the surface and thus air quality [e.g. Schäfer et al., 2006]. Exposure to large concentrations of atmospheric fine particulate matter has negative effects on human health [Ibald-Mulli et al., 2002, Pope et al., 2002, Kappos et al., 2004, Dominici et al., 2006], so accurate modelling of air quality is important, especially in highly populated areas that are prone to situations where the dispersion of aerosols is impeded [Rappenglück et al., 2000, Kossmann and Sturman, 2004]. The prediction of low level turbulence is also important for air traffic as it can produce hazardous situations during take off and landing [Golding, 2005]. The mixing processes can also modify the vertical and horizontal profiles of many meteorological variables, such as wind, temperature and relative humidity, in the lowest region of the atmosphere [e.g. Businger et al., 1971].

The BL is the lowest layer of the troposphere and it is directly influenced by the surface of the earth. According to the definition in Stull [1988], direct influence means that the BL responds to surface forcings within one hour [Seibert et al., 2000]. Transport processes such as turbulence spread the effect of these forcings throughout the BL. Typically, the BL extends from the surface up to altitudes anywhere between 100 and 3000 metres, depending on meteorological factors, location, time of day, and season. Boundary layer processes are also closely tied to the creation of stratocumulus and fair–weather cumulus clouds [Wood, 2012].

The major driver for the diurnal cycle in boundary layer height (BLH) is the diurnal cycle in the amount of solar heating that reaches the surface, although there are other contributing factors. A commonly referred to schematic by Stull [1988] of the diurnal cycle of a convective boundary layer (CBL) driven by solar heating is shown in figure 1. This schematic describes the typical behaviour of the BL and its sub–layers in fair–weather situations when not under the influence of large–scale synoptic weather patterns such as fronts.

The mixing layer (ML) forms the bulk of the daytime BL shown in figure 1. It is characterized by turbulent eddies that mix various quantities (such as potential temperature, relative humidity and aerosol concentration) throughout its whole volume. The eddies are convective and driven by the sensible heat flux at the surface, with the intensity of thermal turbulence being the most defining factor of the mixing layer height (MLH). The ML begins to grow after sunrise and reaches its peak altitude around mid–afternoon. Above the ML there is usually a potential temperature inversion

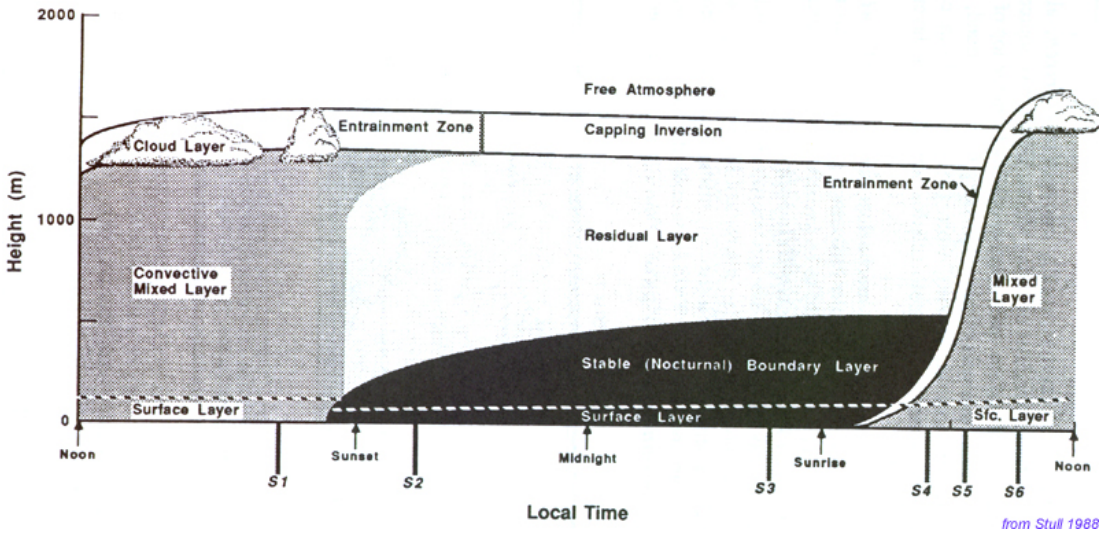

Figure 1: A schematic of the diurnal cycle of a convective bounday layer [Stull, 1988].

(capping inversion) that restricts further mixing. At this interface is the entrainment zone (EZ), which separates the ML from the free troposphere above. The ambient aerosol concentration usually falls rapidly in the EZ, from the high concentrations in the ML into which most pollutants are released to, to the free atmosphere which is quite clean.

Around sunset, there is no more surface heating (no input of sensible heat flux) and convection switches off rapidly with the ML decaying into a residual layer (RL). As the surface starts to cool, a stable nocturnal boundary layer (NBL) forms near the surface and is characterized by weak turbulence.

In more complex situations (with for example low–level cloud cover, low solar zenith angle, high wind shear, frontal activity, geographical forcings, or the presence of anthropogenic heat sources) the BL structure may differ substantially from the standard CBL diurnal cycle [Casadio et al., 1996, Lemonsu et al., 2006]. Assuming a standard diurnal BL cycle as given in figure 1 in these situations is not appropriate: urban heating can generate a shallow convective layer even during the night; a low level jet induces shear–driven turbulent layers; marine and stratocumulus–topped environments may show little or no diurnal cycle.

Turbulence can be explained in terms of local high-frequency variations of the wind superimposed on the mean wind. These variations are combinations of eddies of different sizes. The mechanisms responsible for creating turbulence may be buoyancy–driven

(convection) or mechanically–driven (friction, shear). Convective (thermal) eddies occur when unstable temperature gradients are present, which can be as a result of solar or anthropogenic heating of the surface, or from radiative cooling at cloud top. Frictional eddies are created by obstacles, rough surfaces and wind shear. In the BL, these turbulent eddies can distribute the effect of surface forcings throughout the ML and mix locally–released aerosols.

The aim of this study was to use Doppler lidar measurements to study spatial and temporal variations in turbulent mixing, especially under circumstances which could be more prone for non–standard mixing processes. Understanding of the behaviour of more complex mixing processes in the BL is important for accurate BL and air quality modelling [White et al., 2009]. The mixing processes also affect aerosol formation [Kulmala et al., 2001, Nilsson et al., 2001], and CO_2 exchange rates between forest and the atmosphere [Hollinger et al., 1994].

Various instruments have been used to study turbulent mixing in the BL. In–situ measurements based on masts [Vesala et al., 2008, Wood et al., 2010], tethered balloons [Siebert et al., 2003], aircraft [Khelif et al., 1999, Bange et al., 2007], and unmanned aerial vehicles [Dias et al., 2012, Martin et al., 2014] are capable of producing robust time–series but are point measurements and generally lack the ability to provide a vertical profile simultaneously throughout the whole BL. Active remote sensing instruments such as wind profilers [Angevine et al., 1998], sodars [Beyrich and Görsdorf, 1995], and Doppler lidars [O'Connor et al., 2010, Träumner et al., 2011, Schween et al., 2014, Vakkari et al., 2015] have become increasingly important in studying BL dynamics as they are able to produce simultaneously measured profiles in the line–of–sight direction of the instrument.

In this study turbulent profiles measured with a Doppler lidar were combined with in–situ derived turbulence and meteorological data. The multi–instrument approach allows for more comprehensive understanding of the turbulent phenomena observed, while the meteorological data helps to explain the causes behind the more complex turbulence patterns. The measurement site and the instruments used are described in section 2. The methods applied to the Doppler lidar and the in–situ datasets are presented respectively in sections 3.1 and 3.2. The results are presented in section 4.

2 Measurements

2.1 Site

All measurements in this study were obtained at the Hyytiälä forestry field station, located 61°50'44"N 24°17'19"E in southern Finland. The site is continental and lies about 180 m above sea level. The surrounding environment of the site is rural boreal forest and it is located 60 km north–east from the nearest large city Tampere (230 000 inhabitants, 2016). The location means that low atmospheric aerosol loading is typical and thus the lidar signal tends to be weak. The consequences of this are discussed in section 3.1. The monthly average temperature ranges from -7.7 °C in February to 16 °C in July, with the annual average being 3.5 °C. The average monthly rainfall ranges from 35 mm to 95 mm with an annual average rainfall of 711 mm over 202 rainy days.

The station has been used for forestry research since 1910. Atmospheric research started in the mid–1980s as the site was located in a fallout zone of the Chernobyl nuclear accident. Measurements with SMEAR–II (Station for Measuring Ecosystem - Atmosphere Relations) began in 1995 [Hari and Kulmala, 2005]. Since then, several important discoveries related to secondary aerosol formation have been made at the site [Petäjä et al., 2016].

The station is located between a narrow lake to the west and a ridge to the east as shown in figure 2. An elevation map of the surrounding area is shown in figure 3. Doppler lidar measurements have been performed at the site since December 2012 [Hirsikko et al., 2014], and the instrument was installed on the top of a building, 5 m above the local ground level, so that it could perform unimpeded low–level scanning across the lake. The Doppler lidar forms part of the Finnish meteorological Doppler lidar network operated by FMI. The measurement mast is located on the ridge approximately 400 m to the east from the lidar. The mast was extended from 72 m to its current 125 m height in 2010, although measurements of wind, temperature and humidity at the top of the mast began two years later. The mast lies within the forest so that the first two measurement levels are within the forest canopy.

2.2 Doppler lidar

Doppler lidar (light detection and ranging) is an active remote sensing instrument that measures the radial Doppler velocity and backscattering of atmospheric particles with high temporal and spatial resolution. The outgoing signal is emitted by a laser with a specific wavelength, usually within the ultraviolet, visible, or infrared spectral

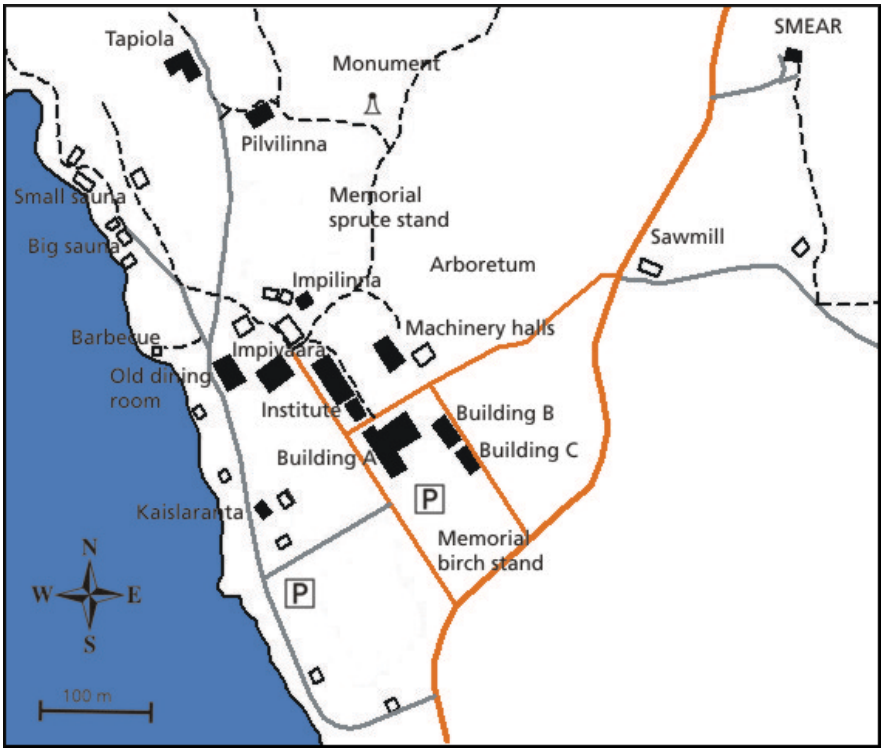

Figure 2: Map of the Hyytiälä forestry field station. The measurement mast is located at the SMEAR site at the north–eastern corner of the map. The Doppler lidar is located on a Machinery hall building at the centre of the map (http://www.helsinki.fi/hyytiala/english/eng_aluekartta.html).

region, and the return signal is sampled to provide a range–resolved profile, similar to a radar. The wavelengths used are significantly shorter than those in radars, making Doppler lidars more sensitive to smaller particles such as aerosols or cloud droplets. Since aerosols and cloud droplets have very small terminal fall velocities, they act as tracers of the air motion; measuring the particle radial velocities is then equivalent to measuring the air radial velocity.

As the velocity measured is the motion along the line–of–sight of the instrument (the direction of the lidar beam), scanning versions of these instruments allow the orientation to be changed to measure various components of the 3–dimensional wind field. Vertical–staring mode where the lidar beam is aligned to zenith provides vertical winds. Horizontal winds are obtained by performing a sequence of scans off–zenith to obtain the horizontal components from which a vertical profile of the horizontal wind can be derived.

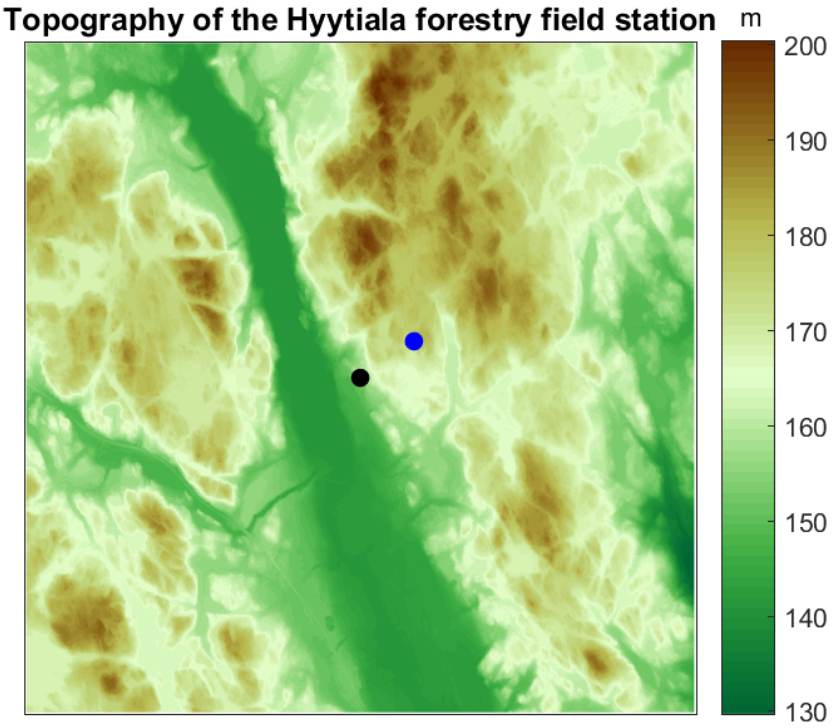

Figure 3: Elevation map of the Hyytiälä forestry field station. The locations of the Doppler lidar and the measurement mast are respectively indicated with a black and a blue dot.

There are two options for obtaining the range information, which depends on whether the laser is pulsed or continuous. For a continuous emission laser the range–resolved information is obtained by changing the focus of the laser beam to maximise the amount of signal expected at a given height. These instruments require very little power to operate, and are relatively simple in design so they are very robust, but are limited in range to about 250 m. Extending the laser focus beyond about 250 m means that the range–weighting function becomes very broad and the retrieval of range–resolved information is no longer possible with this method. For pulsed systems, the return signal is sampled at very rapid time intervals, and the profile in range is calculated from the time elapsed between the transmission and the sample time:

$$R = c\tau/2, \tag{1}$$

Table 1: Doppler lidar specifications for the instrument deployed at Hyytiälä. The instrument is a Halo Photonics Streamline.

Wavelength	1.5 μm
Pulse repetition rate	15 kHz
Nyquist velocity	19.8 m s^{-1}
Sampling frequency	50 MHz
Points per range gate	10
Range resolution	30 m
Pulse duration	0.2 μs
Lens diameter	6 cm
Divergence	33 μrad
Antenna	monostatic optic-fibre coupled

Table 2: Doppler lidar operational scan specifications for the instrument deployed at Hyytiälä.

Scan type	Vertical stare	VAD	DBS
Elevation angle	90°	30°	70°
Number of beams	1	23	3
Pulses averaged	90 000	90 000	60 000
Integration time	6 s	6 s	4 s
Focus	2 000 m	500 m	2 000 m
Repeat time		30 min	30 min

where R is the range, c is the speed of light and τ is the time elapsed. Similarly, the physical range resolution of the instrument is determined by how rapidly the signal is sampled using the same equation; sampling every 200 ns gives a range resolution of 30 m. However, the maximum realistic resolution for the information present in the signal depends on the pulse length, again given by equation 1, obtaining measurements at a higher resolution than the pulse length, known as oversampling, does not result in more information. In practice, Doppler lidars do oversample, and typically oversample by a factor of 10 relative to the pulse length, but essentially this is to obtain more samples from the same pulse. A number of samples are then averaged in range to give an output resolution that is closer to the pulse length. Note that the output resolution does not have to match the pulse length [Rye, 1979, Rye and Hardesty, 1993].

For all Doppler lidar systems, sensitivity (reduced uncertainty) is improved by aver-

aging (or integrating) a large number of profiles together which simultaneously reduces the temporal resolution. The amount of integration depends on the laser output power and the application for which the Doppler lidar is being used for. While high–power lidars require less averaging in time for the same sensitivity as a low–power system, in many cases low–power systems are used because of other practical advantages, such as an eye–safe laser, price, and stability. Besides ground–based observations, Doppler lidars can also be deployed on aircraft or on satellites [Wandinger, 2005].

The specific settings of the Doppler lidar, such as the wavelength, power, focus and pulse repetition frequency, can vary greatly depending on the application. The specifications of the Doppler lidar used in this study are given in table 1. This instrument is eye–safe and operates in a high–frequency low–power mode, averaging lots of samples to obtain sensitivity. Some settings change depending on the scan–type employed (see table 2).

The amount of signal that the lidar receives depends on the backscattering properties of atmospheric particles, which also depends on the wavelength of the laser. The backscattering properties can be determined using Mie theory, although it should be noted that this is only approximate for non–spherical scatterers such as ice and dust. For particles with diameters close to or larger than the laser wavelength, the backscattering is proportional to the cross–sectional area of the particle (proportional to diameter–squared), whereas for significantly smaller particles the backscattering is proportional to diameter to the power six (Rayleigh scattering). The amount of scattering may also depend on laser wavelength, with UV and visible instruments also being able to detect scattering from molecules. Particles also cause extinction, again proportional to the cross–sectional area of the particle. If present in significant amounts, the particles can attenuate the beam, with cloud droplets, raindrops and snow being able to attenuate the signal completely. Thus, cloud bases and ice clouds are easy to detect with lidar (high backscatter), but they simultaneously limit any signal from beyond (high extinction).

The Doppler velocity measurements are based on the Doppler shift in the return signal after being scattered by a moving object. Thus, the velocity measurements do not directly depend on the intensity of backscatter. Because of the short wavelength used by Doppler lidars, the Doppler shift is so small (in the order of femtometers) that it is not easy to measure directly [McKay, 1998]. Typically, heterodyne detection is used, in which the signal returning from the atmosphere is combined with a local oscillator signal in the Doppler lidar. The magnitude of the Doppler shift is then derived from the beating of the two signals. Often the two lasers use different wavelengths so that

it is possible to derive also the sign of the Doppler shift and thus the direction of the velocity [Reitebuch, 2012].

The power of the signal returning to the lidar is given by the lidar equation

$$P(R,\lambda) = P_0 \frac{c\tau}{2} A\eta \frac{O(R)}{R^2} \beta(R,\lambda) exp\Big[-2 \int_0^R \alpha(r,\lambda) dr \Big], \quad (2)$$

where P is the received power, R is the distance between the lidar and the scatterer, λ is the wavelength of the laser, P_0 is the power of the outgoing pulse, c is the speed of light, τ is the temporal pulse length, A is the area of the primary receiver optics, η is the overall system efficiency, O is the overlap function, β is the backscatter coefficient, and α is the extinction coefficient [Wandinger, 2005].

The intensity of the returned signal decreases rapidly as the distance from the Doppler lidar increases. There are two factors to consider: the geometrical fact that the solid angle of the backscattering that reaches the instrument becomes smaller; and attenuation of the signal along the path. The reduction in intensity of the signal does not distort the Doppler velocity measurements, but increases the uncertainty of the measurements until the signal cannot be distinguished from the background noise. The wide range of intensity that the instrument experiences means that the detectors have to have a huge dynamic range. However, very close to the instrument, the backscatter received from the nearest range gates may be so strong that it can saturate the detector. In addition, for pulsed lidars, the trailing end of the outgoing pulse may also be present (the pulse shape is closer to Gaussian than a square wave) so that there is an ambiguity on whether the measured signal is from the transmitted or from the received signal. Thus, there is always a data gap between the instrument and the nearest available measurement. For the instrument considered here, this means a blind zone in the nearest 100 m or so. Hence, for vertical–pointing measurements, there is no information until above 100 m in altitude. This minimum altitude can be reduced by performing scanning at lower elevations (although the minimum range is still 100 m). Such scans also provide better vertical resolution but the temporal resolution of the full scan is lower. Scanning at low elevation may also suffer from more attenuation along the beam.

2.3 Winds

The two most commonly used scan types to retrieve profiles of horizontal winds are Velocity Azimuth Display (VAD) and Doppler Beam Swinging (DBS). Both methods use trigonometry to obtain the horizontal component of the wind from the measured radial velocity, and the retrieval assumes horizontal homogeneity [Menzies and Hard-

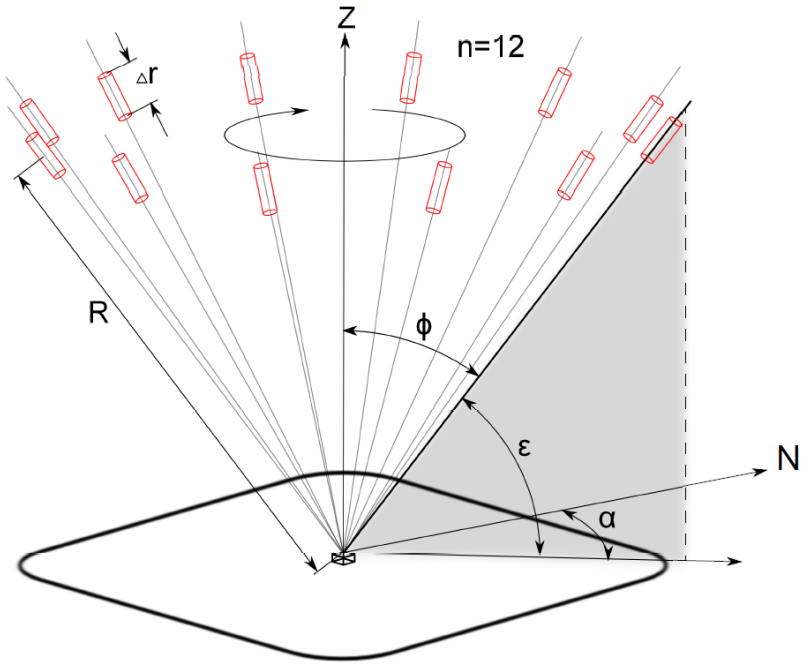

Figure 4: The geometry of a VAD scan with 12 beam directions. ε is the elevation angle and α is the azimuth angle. The rotation is performed around the Z-axis. Δr denotes the pulse length [Päschke et al., 2015].

esty, 1989, Lane et al., 2013]. VADs are done by performing a full rotation in respect to the azimuth with a constant elevation angle. The resulting measurement pattern is an upside down cone such as the one shown in figure 4. The VAD scan can be performed with a continuous rotation resulting in each pulse having their own azimuth angle. The other option is to select a set of azimuth angles and dwell at each azimuth angle for a set period of time (step–stare). The advantage of the step–stare method is that it is much easier to modify the number of beams and dwell time to achieve the sensitivity required, and calculate the uncertainties. A typical step–stare VAD scan consists of at least 12 beams with different azimuth angles, with more beams improving the retrieval.

A DBS scan can be performed with three, four or five beams. The 3 beam method uses one vertical beam with two slanted beams towards north and east. The 5 beam method adds beams slanted towards south and west to the 3 beam method. The 4 beam method uses only slanted beams with no vertical beam. Due to the smaller number of beams required, DBS scans are faster to perform than VADs, but are not as robust as they are more susceptible to turbulence invalidating the retrieval assumption.

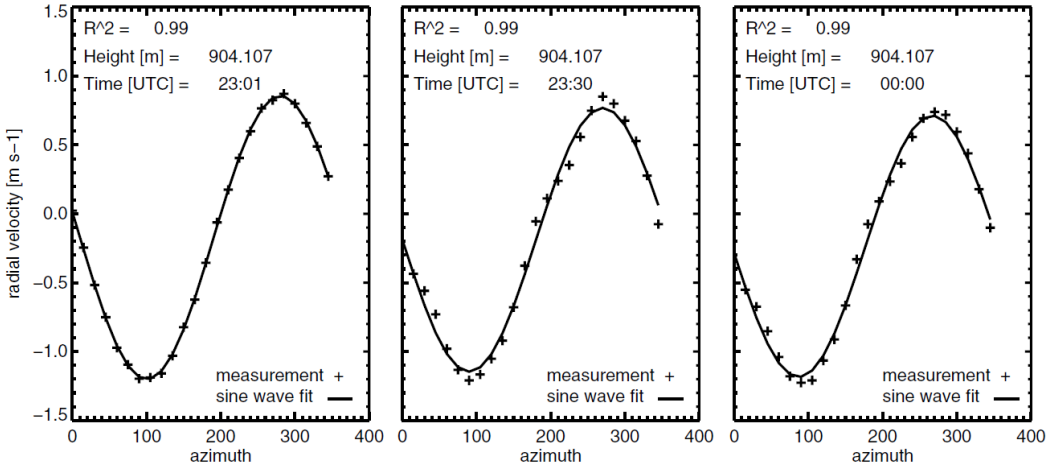

Figure 5: Examples of sinusoidal fits over radial velocity measurements from Lindenberg. Adapted from Päschke et al. [2015].

While the retrieval of vertical velocities is rather straightforward by having the Doppler lidar measure in the vertical staring mode, the derivation of the horizontal winds requires more processing. As the VADs provide radial velocity measurements in conical patterns, the problem of determining the horizontal wind components becomes more demanding. The wind field is assumed to be horizontally homogeneous and stationary, resulting in an expectation that the radial velocity measurements should follow a sinusoidal curve across all of the azimuth angles (see figure 5). A robust method of solving the individual wind components (u, v, w) from the radial velocities is given by Päschke et al. [2015]

$$\boldsymbol{Av} = \boldsymbol{V}_r, \tag{3}$$

where $\boldsymbol{v} = (uvw)^T$, $\boldsymbol{V}_r = (V_{r1}, V_{r2}, V_{r3}...V_{rn})^T$ with V_{ri} being the ith measured radial velocity and n is the number of beam directions in the scan. $\boldsymbol{A}$ is a matrix of unit vectors of the beam directions

$$\boldsymbol{A} = \begin{pmatrix} sin(\alpha_1)sin(\phi) & cos(\alpha_1)sin(\phi) & cos(\phi) \\ sin(\alpha_2)sin(\phi) & cos(\alpha_2)sin(\phi) & cos(\phi) \\ sin(\alpha_3)sin(\phi) & cos(\alpha_3)sin(\phi) & cos(\phi) \\ ... & ... & ... \\ sin(\alpha_n)sin(\phi) & cos(\alpha_n)sin(\phi) & cos(\phi) \end{pmatrix}, \tag{4}$$

where α_i is the azimuth angle and ϕ is the elevation angle of the scan. As $\boldsymbol{A}$ is determined by the scan settings and $\boldsymbol{V}_r$ is the measured radial velocities, the individual wind components can be solved from equation 3 using the method of least squares. The retrieval by Päschke et al. [2015] also provides uncertainties, a measure of the goodness–of–fit, and a condition number of the matrix $\boldsymbol{A}$. The goodness–of–fit and condition number are used to determine whether the assumption of homogeneity can be made, which is often not the case in strongly turbulent conditions.

The Doppler lidar used in this study provides operational winds from both VAD and DBS scans (see table 2 for specifications), with the VAD scans providing higher vertical resolution close to the surface. In addition the VAD scans can be used to study spatial representativity.

2.4 Mast

The meteorological variables used for comparison with the Doppler lidar data were measured at various altitudes on a 125 m high measurement mast (figure 6). All of the datasets described in this subsection are available at https://avaa.tdata.fi/web/smart. Temperature was measured with Pt100 resistance thermometers at 4, 8, 16, 33, 50, 67 and 125 metres above ground level. The 4 and 8 m measurements lie within the surrounding forest canopy. Results from some of the thermometers indicate that there are probably some calibration issues with the instruments. Section 3.2.3 contains further discussion on how this issue was addressed. Relative humidity (RH) was measured at 16, 67 and 125 metres above ground level. RH at 16 m was derived from a dew point measurement and the respective temperature measurement, while RH at 67 and 125 m were measured with Rotronic MP102H RH sensors. The RH sensors can be attached to the Pt100 thermometers, but it is unclear whether it is the case. The 67 m RH measurement does occasionally show full saturation in situations where neither of the other measurements indicate such condition, suggesting that the RH measurements could be affected by inaccurate thermometers. Horizontal wind speed and direction was measured with Thies 2D Ultrasonic anemometers at 8, 16, 33, 67 and 125 metres above ground level. Ground level atmospheric pressure was measured with a Druck DPI 260 barometer. The temporal resolution of the measurements was 1 minute.

In addition to the meteorological quantities, latent and sensible heat fluxes were measured. Both measurements were performed at 23 metres above ground level. The sensible heat flux was measured with a Gill Solent 1012R anemometer/thermometer with the latent heat flux obtained by including a LI–COR LI–6262 gas analyzer.

Figure 6: The measurement mast at the Hyytiälä forestry station. Photo courtesy of Juho Aalto.

The sensible heat flux, H_S, is defined as

$$H_S = \overline{\rho_d} c_p \overline{w'\theta'_s}, \tag{5}$$

where $\overline{\rho_d}$ is the average density of dry air, c_p is the specific heat capacity of air at constant pressure and $\overline{w'\theta'_s}$ is the covariance between the fluctuations in vertical velocity of the air w' and the fluctuations in sonic temperature θ'_s [e.g. Rebmann et al., 2012]. The latent heat flux, H_L, is defined as

$$H_L = L_E \overline{w'q'}, \tag{6}$$

where L_E is the latent heat of evaporation for water and $\overline{w'q'}$ is the covariance between the fluctuations in vertical velocity of the air w' and the fluctuations in the specific humidity of the air q' [e.g. Large and Pond, 1982]. The temporal resolution of the fluxes is 30 minutes.

Other meteorological variables were calculated from the measured quantities. Section 3.2.2 describes the derivation of potential temperature Θ, which is defined as

$$\Theta = T\left(\frac{P_0}{P}\right)^{\frac{R}{c_p}} \tag{7}$$

where T is the temperature at a chosen altitude, P is the air pressure at the respective height, P_0 is 1000 hPa, R is the gas constant of air and c_p is the specific heat capacity of air at constant pressure.

Dissipation rates, used as a measure of turbulence, were derived in the same way as for the Doppler lidar measurements, and the procedures are described in section 3.2.1.

2.5 Measurement period

The data for this study was measured between 2nd September 2015 and 7th August 2016. The Doppler lidar data from November 2015 to February 2016 contains high amounts of precipitation, fog and low level clouds, and is therefore not suitable for the purposes of this study. There are no wind measurements from the mast at 125 m before 18th October 2015 and from 67 m before 5th November 2015. For the rest of the measurement period, the availability of data was above 90 % for most days. Due to these limitations of the datasets, most of the research concentrated on data from the spring and summer of 2016.

3 Methods

3.1 Lidar data processing

3.1.1 Background correction

As the intensity of the lidar return signal is proportional to the amount of aerosol in the atmosphere (equation 2), the signal–to–noise ratio (SNR) of the Doppler lidar measurements tends to be smaller in less polluted areas. The measurements for this study were performed in a such a remote and clean location that using standard threshold values of SNR [e.g. Pearson et al., 2009, Päschke et al., 2015] to discard noisy signals would drastically diminish the amount of data available. In order to increase the size of the usable dataset, the background signal of the measurements was corrected using the method of Manninen et al. [2016]. This improves the background determination performed internally by the instrument through removing ripples in the calibration background scan, removing offsets, and accounting for non–constant offsets. The SNR threshold value can then be decreased by as much as a factor of 4.

3.1.2 Turbulence calculation

The dissipation rate of turbulent kinetic energy was calculated as a representative measure of turbulence. For vertically–pointing measurements, the equation given by O'Connor et al. [2010] was used:

$$\epsilon = 2\pi \left(\frac{2}{3a} \right)^{3/2} \sigma_{\bar{v}}^3 (L^{2/3} - L_1)^{-3/2}, \tag{8}$$

where ϵ is the dissipation rate, $a = 0.55$ is the Kolmogorov constant, $\sigma_{\bar{v}}^2$ is the variance of the Doppler velocity calculated from N samples, $L = NUt$ is the length scale with U and t respectively being the horizontal wind speed and the dwell time, and L_1 is the length scale for one sample. Equation 8 assumes that the largest length scales measured, L, still lie within the inertial subrange. Since L typically scales with the boundary layer depth, ranging from about 0.5–1.5 km, this puts an upper limit on the maximum integration time, as enough samples (at least 10) are needed to create a reliable variance. For light wind speeds, this dictates that the total time over which the variance is derived should be less than three minutes, and that the total time should be reduced at higher wind speeds. In practice, the variance is created with a temporal resolution higher than 2 minutes, so that it is almost always appropriate to assume that all length scales measures are within the inertial subrange. The O'Connor et al. [2010]

algorithm also provides uncertainties in the retrieved ϵ values. Gaps in the vertical profile of ϵ occur when SNR is too low, or the uncertainty in ϵ is too high.

3.1.3 Turbulence from scans

As a part of its measurement schedule, the Doppler lidar performed VAD scans at an elevation angle of 30° from horizontal. From these VAD30 scans turbulent profiles were calculated using the method described by Vakkari et al. [2015]. The method is different to that used for the vertical staring mode because of the temporal limitations of the VAD30 datasets. As the scans are performed only once every 30 minutes, there is no continuous time series over which turbulence could be calculated using equation 8. It is also not viable to compare the radial velocity measurements at the same range gate from sequential beams, because, due to the conical shape of the scan, the data points are so far away from each other that the assumption of horizontal homogeneity and stationarity are no longer likely to be valid. Instead the calculation of turbulence (σ^2_{VAD}) is based on the variance of the residuals between the measurements and the sinusoidal radial velocity fit for homogeneous horizontal winds from two consecutive range gates. Thus the distance between the data points that are being compared is only 30 m. Similar to the vertical–pointing retrieval method, there are gaps in the turbulent profile retrieved by scanning when SNR is too low.

3.1.4 Directional turbulence from scans

As the terrain surrounding the Doppler lidar is not homogeneous, this provided an incentive to study whether spatial differences in turbulence, especially during the growth of the ML, could be detected. To study this, turbulent profiles for each individual beam direction of a VAD30 scan were calculated. The method that was used is exactly the same as for calculating the σ^2_{VAD} except that the final averaging of the results to a vertical profile was not performed. The removal of this last step has a downside, as it also increases the uncertainty of the results. The consequences are visible in the results of the directional σ^2_{VAD} as the proportion of neglected data points has notably increased in comparison to the regular σ^2_{VAD}.

3.1.5 Mixing layer height detection

MLH was calculated for all turbulent profiles measured with both the vertical–staring mode and the scanning mode (VAD30). Wavelet transformation was first tested for the detection of MLH, but it failed to provide satisfactory results. During the day, the

turbulent profile often showed strong turbulence all the way to the top of the available measurements. This poses problems for the wavelet method as it requires several data points on both sides of a step change for it to be recognisable. Instead of the wavelet method, a dynamically–calculated threshold value was used. After experimenting with different ways of calculating the threshold value, the equation that was found to provide the most consistent results was

$$\epsilon_{Lim} = \epsilon_{Med} - a\epsilon_{STD}, \tag{9}$$

where ϵ_{Lim} is the threshold value, ϵ_{Med} is the median value of the vertical turbulence profile, $a = 0.05$ and ϵ_{STD} is the standard deviation of the profile. The value of a was derived by experimentation and it has no physical foundation. However, experimentally derived constant threshold values have been used in MLH detection before [Tucker et al., 2009, Vakkari et al., 2015]. As the threshold value used is this study is dynamic it is more robust in detecting NBLs, which tend to be weaker than daytime MLs, than a constant value.

MLH was assigned to be one range gate below the lowest instance where $\epsilon < \epsilon_{Lim}$. If no such value was found, the MLH was assigned to the profile top. Cases where the MLH is defined to coincide with the profile top should be considered as a minimum bound on MLH, since it is not obvious that the loss of signal necessarily indicates the transition from a turbulent BL to the free atmosphere.

3.2 Mast data processing

3.2.1 Turbulence calculation

To evaluate the turbulent profiles retrieved from the Doppler lidar, turbulence was also calculated from the anemometer measurements on the mast. The same equation (8) was used to attain as coherent datasets as possible. Note that there are still some physical differences between the two measurement types. Doppler lidar provides volume measurements in contrast to the point measurements provided by an anemometer. Turbulence from the Doppler lidar is based on vertical velocities (vertically–pointing data) or radial velocities (scanning data), while turbulence from the mast utilizes the magnitude of the horizontal wind. As the temporal resolution of the anemometer data used in this study is lower than that of the Doppler lidar data, the length scale and the temporal interval of the calculations are necessarily larger in order to include enough samples. The calculations were performed with 10 samples with 1 minute temporal

resolution. The resulting 10 minute interval is longer than desired but using a smaller number of samples can distort the results. Despite the differences in the magnitudes and the directions of the input values, the resulting turbulent patterns in the two datasets are very similar (see section 4.1).

3.2.2 Potential temperature calculation

Potential temperature was calculated from the temperature and the ground level pressure measurements. The full calculation includes taking the relative abundance of water vapour into account, but the magnitude of this effect was negligible compared to the uncertainties in the temperature measurements. Since RH measurements were not always available, the impact of water vapour was not taken into account in order to increase the amount of data available. The density of the layer of air between ground level and the temperature measurement was assumed to be constant to aid derivation of the pressure at the height of the temperature measurement (pressure is only measured at the surface). This assumption is not ideal but, as the depth of the air column is limited to the height of the mast, the potential error arising from this assumption is much smaller than the uncertainties in the measurements themselves. The maximum possible error of these assumptions was calculated by selecting the most error prone situation during the whole measurement period and performing the calculations with the largest possible error in the assumed values, (i.e. taking the warmest temperature measured and assuming 100% RH at the top of the mast). The maximum error calculated in this manner was $< \pm 0.05°C$ and so the simplifications used here can be considered reasonable.

The pressure at the height of the mast temperature measurement was obtained from

$$P = P_{surf}\left(1 - \frac{gh}{RT}\right)^{-1}, \tag{10}$$

where $g = 9.81$ m s^{-2} is the gravitational acceleration, h is the height at which the pressure is calculated and P_{surf} is the measured surface pressure. Once the pressure at mast temperature measurement height was obtained, the corresponding potential temperature was calculated with equation 7.

3.2.3 Applications of potential temperature profiles

Vertical profiles of potential temperature are great indicators of atmospheric stability and indicate whether the BL is well mixed. As potential temperature data was available

at several different altitudes (see sections 2.4 and 3.2.2), it was possible to calculate the growth rate of the ML during the morning. Potential temperature from 4 and 8 m heights were not included for these calculations as these heights are within the forest canopy and thus their behaviour will differ from the rest of the profile. The 16 m potential temperature was used for comparison with other altitudes and it was assumed to be always well mixed as it would always be within the surface layer (where turbulent mixing is produced by shear). Examination of the turbulent time series at 16 m shows that this assumption is reasonable. Potential temperatures above this height (33, 50, 67 and 125 m) were used for calculating the growth rate of the ML.

As mentioned in section 2.4, issues in the calibration of the thermometers were noticed. This can be seen in figure 11, where the potential temperatures at 33, 50 and 67 m are 1-2 °C lower than those at other heights, even though the situation is clearly well mixed (corroborated by the Doppler lidar data). It is not possible to calculate a growth rate from these measurements without taking these calibration issues into account. The calibration was performed by calculating and adding a constant offset value for each 24 h time–series. The offsets were obtained by assuming that at 12:00 UTC (which corresponds to less than 2 hours after local solar noon) the situation would be well mixed. Constant values were added to the time–series at each altitude so that they would all have the same value at 12:00 UTC as at 16 m. It was difficult to find a consistent single factor explaining the temperature calibration issues and further investigation is required. However, the calibration method employed here was sufficient for the purposes of this study which was only concerned with relative differences in potential temperature.

Small fluctuations in the time–series were smoothed by applying a 60–minute median filter. All time series were then scaled with respect to the 16 m time–series, after converting the data to kelvins, which also helps to avoid numerical issues. Based on observed diurnal cycles during standard CBL cases, the assumption was made that a time–series is well mixed when the scaled value was 1 ± 0.002. The value of the scaled 16 m time–series is always 1 (see figure 16). The growth rate of the early morning ML was obtained by assuming that the ML had grown to a particular altitude once the scaled time–series indicated a well mixed situation.

4 Results

In this section we show results from two case studies. The first case study concerns a day with typical CBL structure and a low–level jet in the evening. The second case study shows the effect of a frontal system passing. Spatial variability in turbulence is also investigated as is the atmospheric stability close to the surface.

4.1 Case study 1

The following case study of 24th May 2016 portrays how vertical velocity data from the Doppler lidar can be combined with VAD scans and in–situ mast data to gain a more thorough understanding of the state of the atmosphere. The day was mostly cloud free. Sunrise was at 01:07 UTC and sunset at 19:32 UTC, with solar noon at 10:19 UTC.

Figure 7 shows dissipation rates derived directly from vertically–pointing Doppler lidar radial velocities and from the horizontal in–situ measured winds on the mast. The two measurement systems display slightly different portions of the BL, the mast from the surface to 125 m and the Doppler lidar from 120 m upwards, and the overall turbulent pattern matches well with each other. The slightly lower values in the in–situ data can be attributed to the different orientation of the winds used. The in–situ measurements fill the gap between the ground and the lowest usable lidar gates, and thus when combined they provide continuous vertical turbulence profiles that extend through the whole BL. As expected, the in–situ measurements show that there is often weak turbulence present near the ground at night that lies below the Doppler lidar measurement limit in the vertical.

The results show a classic deep CBL which is common for a late–spring day with a clear sky. The ML starts growing rapidly around 04:30 with the in–situ data showing that some growth can be seen already from 03:00 UTC onwards. The MLH peaks above 2000 m around 15:00 UTC and from 16:30 UTC onwards it collapses quickly. The MLH detection algorithm seems to work well on this day, although the results are somewhat ambiguous during the collapse of the ML, due to the slow decay of the larger eddies in the middle of the BL.

At 19:30 UTC, about an hour after the CBL turbulence has almost completely died out, it suddenly increases again. The Doppler lidar shows a maximum between 600 and 700 metres, and the in–situ measurements show elevated values between 60 m and the top of the canopy. As the night progresses the turbulent area detected by the Doppler lidar weakens and its altitude decreases slightly. The observed pattern of turbulence resembles that of the regions of shear above and below a nocturnal low–level jet. At

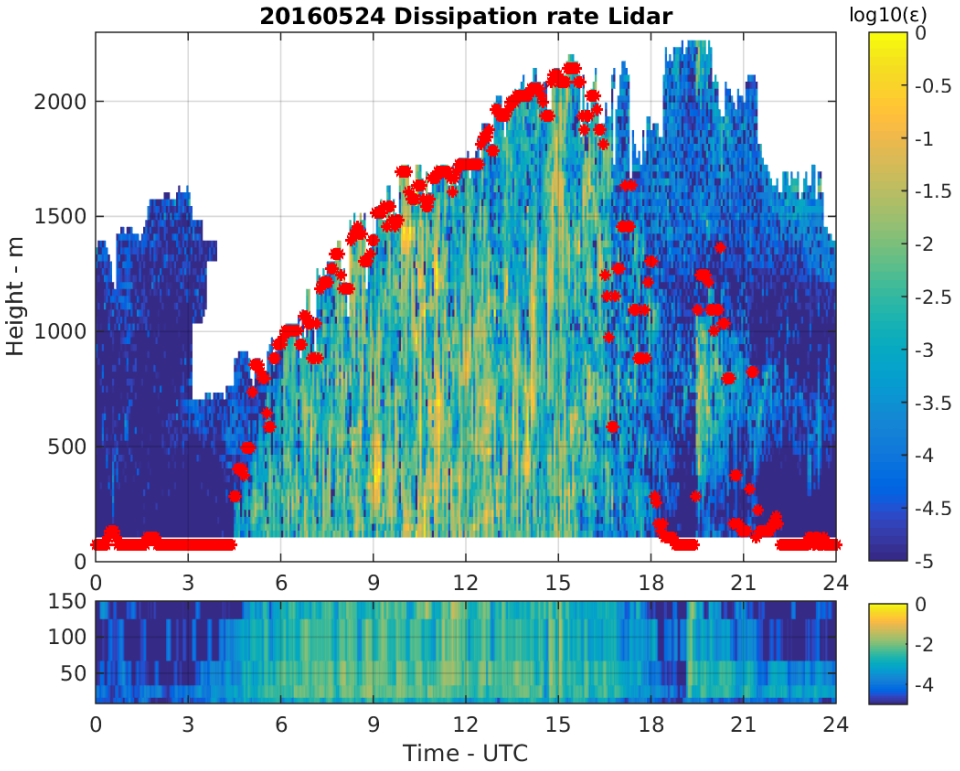

Figure 7: Dissipation rates from vertical velocity data measured by the Doppler lidar (above) and from horizontal wind measurements on the mast (below) at the Hyytiälä forestry field station on 24th May 2016. The log_{10} color scale is same for both of the plots. The red dots represent MLH derived by the algorithm described in section 3.1.5.

the center of the jet the flow is nearly laminar so not turbulent, while above and below it are areas of strong shear.

The horizontal wind speed derived from Doppler lidar DBS scans at an elevation angle of 70° are shown in figure 8b. During the daytime some rather sporadically appearing bursts of high horizontal velocities are detected. When comparing these with the vertical velocities measured by the lidar (figure 8a) it can be seen that the high horizontal velocities at this hour are often associated with strong up- and downdrafts. At the same time fluctuations in the direction of the horizontal velocities are also seen (figure 8c), but as the changes are driven by turbulent eddies, they are random by nature and thus no further connection between the wind components can be found.

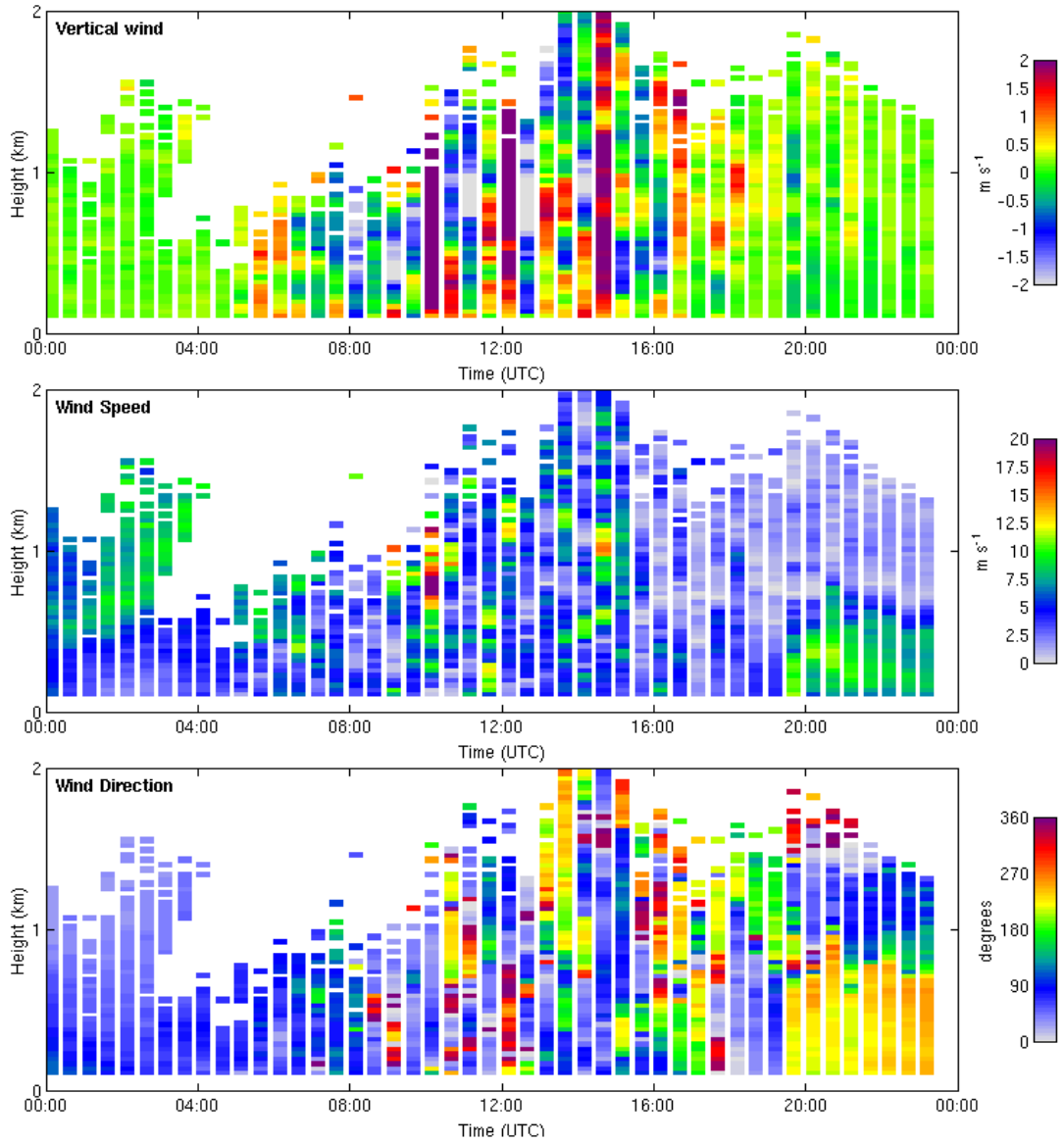

Figure 8: ***a)*** *Vertical wind velocity,* ***b)*** *horizontal wind speed and* ***c)*** *wind direction derived from Doppler lidar DBS scans at an elevation angle of 70° at the Hyytiälä forestry field station on 24th May 2016.*

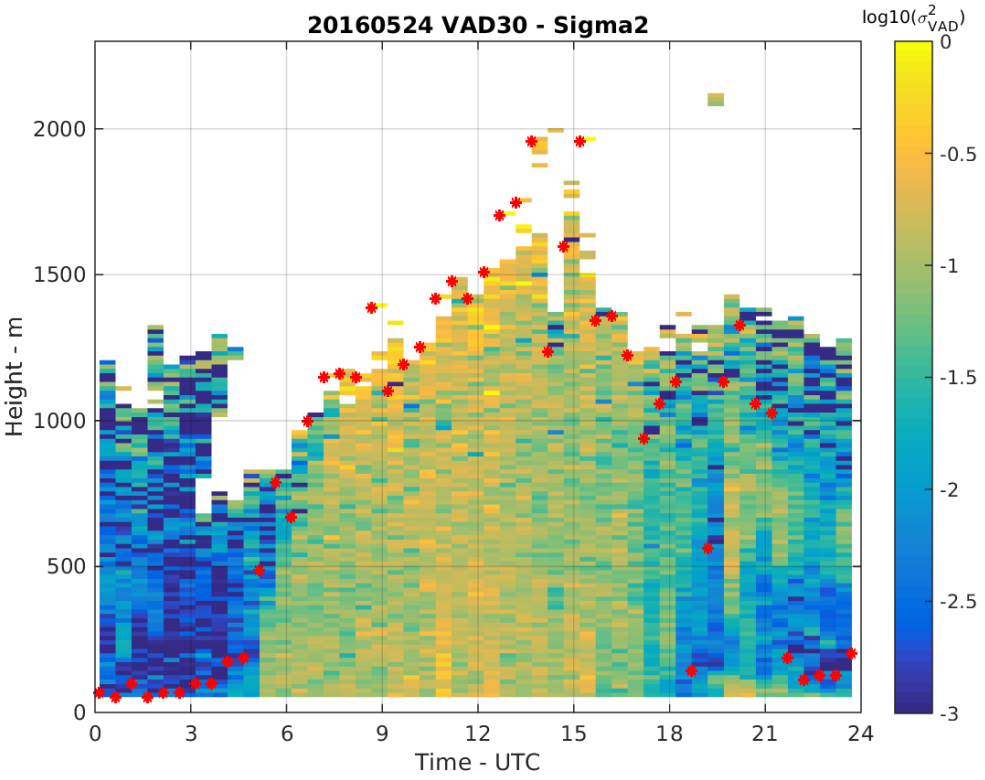

Figure 9: σ^2_{VAD} from Doppler lidar VAD30 scans at the Hyytiälä forestry field station on 24th May 2016. The red dots represent MLH derived by the algorithm.

This is a known problem, where strong turbulence can invalidate the wind retrieval method [Päschke et al., 2015]. Starting at 19:30 UTC, a nocturnal low–level jet can be seen in the horizontal wind data with maximum velocities around the altitude of 300 to 400 m. The strongest vertical gradients in wind speed match the regions of increased turbulence in figure 7. In figure 8c, strong vertical gradients in the wind direction are apparent at the same locations. The direction of the jet is exactly opposite to that of the preceding winds (morning and daytime) and the winds above. Both wind speed shear and wind direction shear contribute to shear–driven turbulence as it is the vector wind shear that is important.

Figure 9 shows σ^2_{VAD} derived from Doppler lidar VAD30 scans described in section 3.1.3. The turbulent behaviour is similar to that seen in figure 7. Due to the lower altitude of the first usable measurement, the Doppler lidar is able to pick up turbulence near the ground that was not seen in the vertical data. The early morning behaviour

of the turbulent layer matches the one seen in the mast data. Low level mixing can seen as early as at 03:00 UTC while the rapid growth of the ML initiates around 04:30 UTC. Even though the MLH detection algorithm is able to detect the collapse of the ML after 18:00 UTC the low temporal resolution of the σ^2_{VAD} makes the transition from the CBL to the nocturnal jet seem almost continuous, effectively pointing out the possibility of misinterpretation in situations where only one observation type is used. For the nocturnal low–level jet, both areas of shear–driven turbulence above and below the jet are now visible in the same measurement.

Because of the slanted propagation path of the lidar pulse in the atmosphere, the VAD30 scan suffers from a greater amount of attenuation by the intervening BL aerosol than the vertical–staring mode. As a result, this prevents reliable detection of the top of deep MLs, which is the case in figure 9. When comparing it to figure 7, it is seen that reliable data for the VAD30 scan does not actually reach the top of the ML, and thus the MLH is underestimated.

Time series of latent and sensible heat fluxes measured on the mast at an altitude of 23 m above ground level are shown in figure 10. During the daytime, the fluxes behave as expected for a deep CBL situation. Both fluxes begin to increase after 03:00 UTC from their near zero nocturnal values. This observation matches with the low level turbulence that can be seen starting around this hour in figures 7 and 9. The fluxes peak about an hour before the local solar noon after which they begin to decrease. By 18:00 UTC the fluxes have weakened to approximately zero, matching the complete collapse of the ML observed in the turbulent plots. At 19:00 UTC, just before the nocturnal jet starts, there are simultaneous spikes in both heat fluxes, negative in the sensible heat flux and positive in the latent heat flux. The reason for this behaviour is unclear and it requires further research. Due to the immediate temporal proximity of the spikes to the start of the nocturnal jet, it seems highly probable that these events are linked with a causal relationship.

In figure 11, potential temperatures measured at various altitudes on the mast are shown. As the 4 and 8 m measurements lie so close to one another in the canopy, they are almost identical throughout the whole time. The night–time period is clearly stable as the potential temperature increases with altitude. From 3:30 UTC onwards the effects of turbulent mixing and ML growth can be seen, as the potential temperatures start to become one by one equal with the measurements below. By 05:00 UTC the potential temperature has become mixed throughout the whole vertical extent of the mast. Comparison with the turbulence derived from the highest in–situ measurements in figure 7, shows that the time it takes for the potential temperature to become well

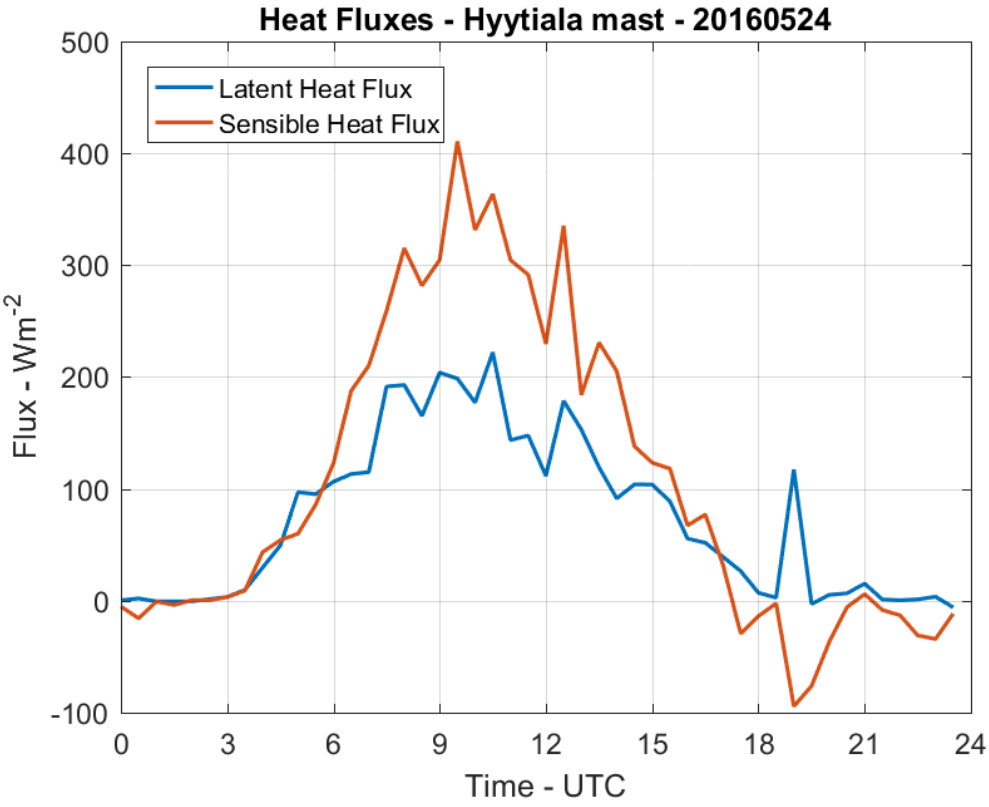

Figure 10: Heat fluxes measured on the mast at 23 m above the ground at the Hyytiälä forestry field station on 24th May 2016.

mixed after the first signs of convective mixing is only a few minutes even at the top of the mast. The time series behave mostly as expected for the prevalent meteorological conditions although some anomalies are also seen. According to the turbulence data (in figure 7) the daytime BL is well–mixed, and thus the lower values of potential temperature observed at 33, 50 and 67 m seem surprising. Further examination of the temperature measurements over the whole measurement period resulted in a conclusion that the disparity is most likely a calibration issue with the thermometers. The discovery of these calibration issues led in part to the development of methods described section 3.2.3.

The potential temperatures increase until 16:00 UTC and then begin to decrease after 17:00 UTC. The lowest levels cool down the fastest and the higher levels become decoupled from the ground, thus indicating that the BL is not well–mixed any more. Between 19:00 and 19:30 UTC rapid changes are observed at all levels. At 4 and 8 m the

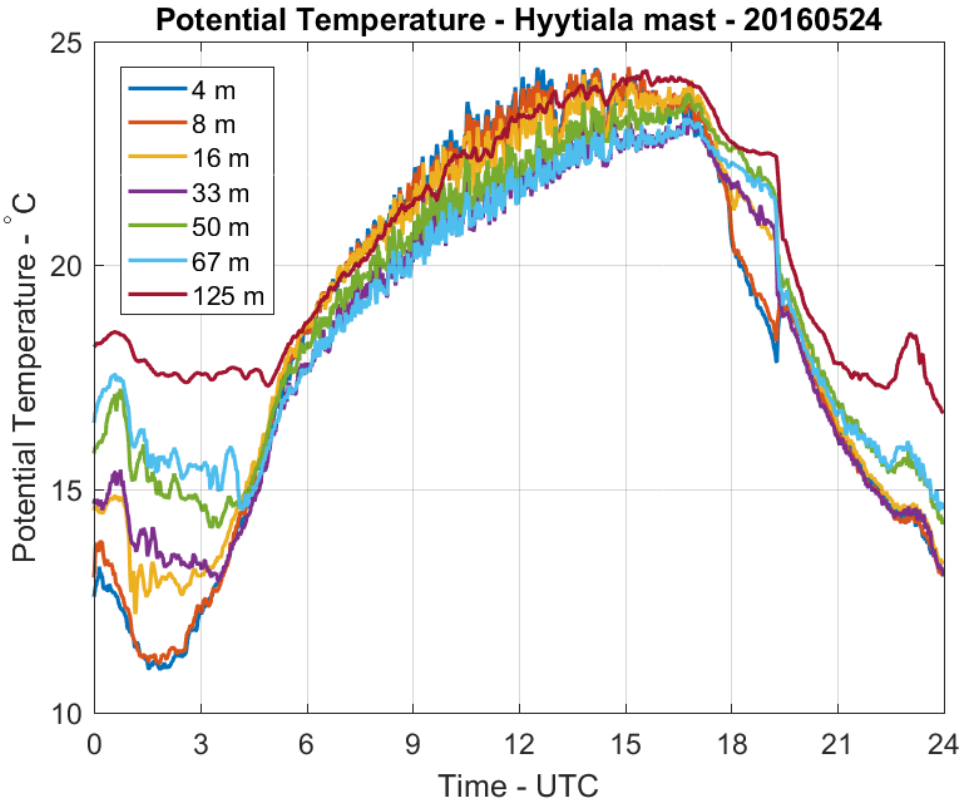

Figure 11: Potential temperatures derived on the mast at various altitudes at the Hyytiälä forestry field station on 24th May 2016.

potential temperatures increases slightly while all the other levels experience decreases of a larger magnitude. The BL seems to have become well-mixed again during this period, although at 125 m the effects of mixing seem to be slightly less pronounced. These changes are all linked to the formation of the nocturnal low–level jet. Later during the night as the nocturnal jet starts to weaken, as can be seen in figure 8, the highest and the lowest measurements begin slowly to decouple from each other. The relative humidity and wind speed measurements (not shown) from the mast display similar behaviour to the results shown here, and thus strengthen the interpretation.

4.2 Spatial differences in turbulence

As the location surrounding the Doppler lidar is topographically diverse, it was investigated whether differences in turbulence and ML growth can be detected with the

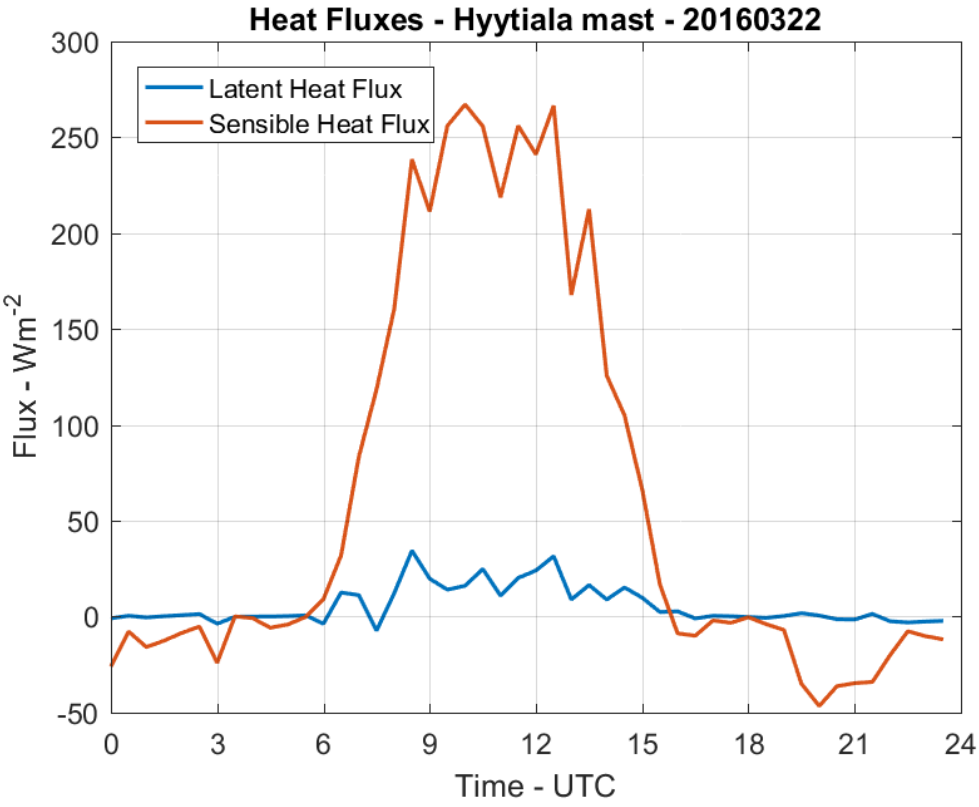

Figure 12: Heat fluxes from measured on the mast 23 m above the ground at the Hyytiälä forestry field station on 22nd March 2016.

VAD30 scans. Of special interest was to identify whether differences in the rate of exchange between the lake and the forest could be observed. Quasi 3-dimensional maps of the turbulent structure were created from directional components of the σ^2_{VAD}, which were obtained using methods described in section 3.1.4. Evaluation of whether the results showed signs of spatial differences was done manually. As expected, no differences were observed during daytime when large scale turbulent eddies are present.

4.2.1 Spatial differences in mixing layer growth

A case of significant spatial differences during the early stages of ML growth was observed on 22nd March 2016. Sunrise occurred at 04:16 UTC and there were no clouds present during the morning or the previous night. The winds were very weak and the temperature ranged from -13°C at the night to -2°C during the day. The clear sky

allowed unimpeded solar heating and radiative cooling of the surface. This can be seen in figure 12, which shows the heat fluxes from the day in question. During the preceding night the sensible heat flux is slightly negative due to the radiative cooling of the surface. Around 06:00 UTC the sensible heat flux begins to increase rapidly and within just over two hours it has reached 200 W m^{-2}. During this period of increase in the sensible heat flux, spatial differences in turbulence and ML growth were observed.

The temporal and spatial development of directional σ^2_{VAD} over a 1.5 hour period is shown in figure 13. At 06:45 UTC weak low level turbulence is detected near the Doppler lidar. Some higher values of σ^2_{VAD} are seen further up in the atmosphere, where there are also many data points missing due to too high uncertainties. At 07:15 UTC the low level turbulence begins to intensify and mixing reaches slightly higher altitudes. The turbulence seems to be somewhat stronger on the north-eastern side above the ridge, while it is weaker and limited to lower levels above the lake on the western side. The differences increase significantly by 07:45 UTC, when the turbulence above the ridge reaches altitudes several times higher than above the lake and the intensities differ by orders of magnitude. At 08:15 UTC the differences are still visible although the deeper ML now has larger–scale turbulent eddies which begin to reduce the spatial differences and make them harder to detect. The results of the 08:45 UTC scan (not shown), indicate that the whole area has become rather uniformly turbulent. No spatial differences were observed during the rest of the day.

4.2.2 Nocturnal differences

During several summer nights, one sector with increased turbulence was detected. The intensity and the altitude which the turbulence reached varied but the radial direction was always the same; on the ridge to the east of the Doppler lidar. No pattern of related wind direction or speed was detected although some cases seemed to be associated with weak nocturnal low–level jets. As the horizontal winds were derived using the method by Päschke et al. [2015], described in section 2.2, it was not possible to retrieve the full 3–dimensional wind field from the Doppler lidar measurements. Thus it was not possible to determine whether, in the cases where no nocturnal jet was detected, there were some small scale flows associated with the areas of the increased turbulence. The timing of the peak intensity of the turbulence varied as much as 6 hours from night to night.

Figure 14 shows directional σ^2_{VAD} derived from VAD scans from four different nights. Figure 14a shows a standard calm night without any significant spatial differences in

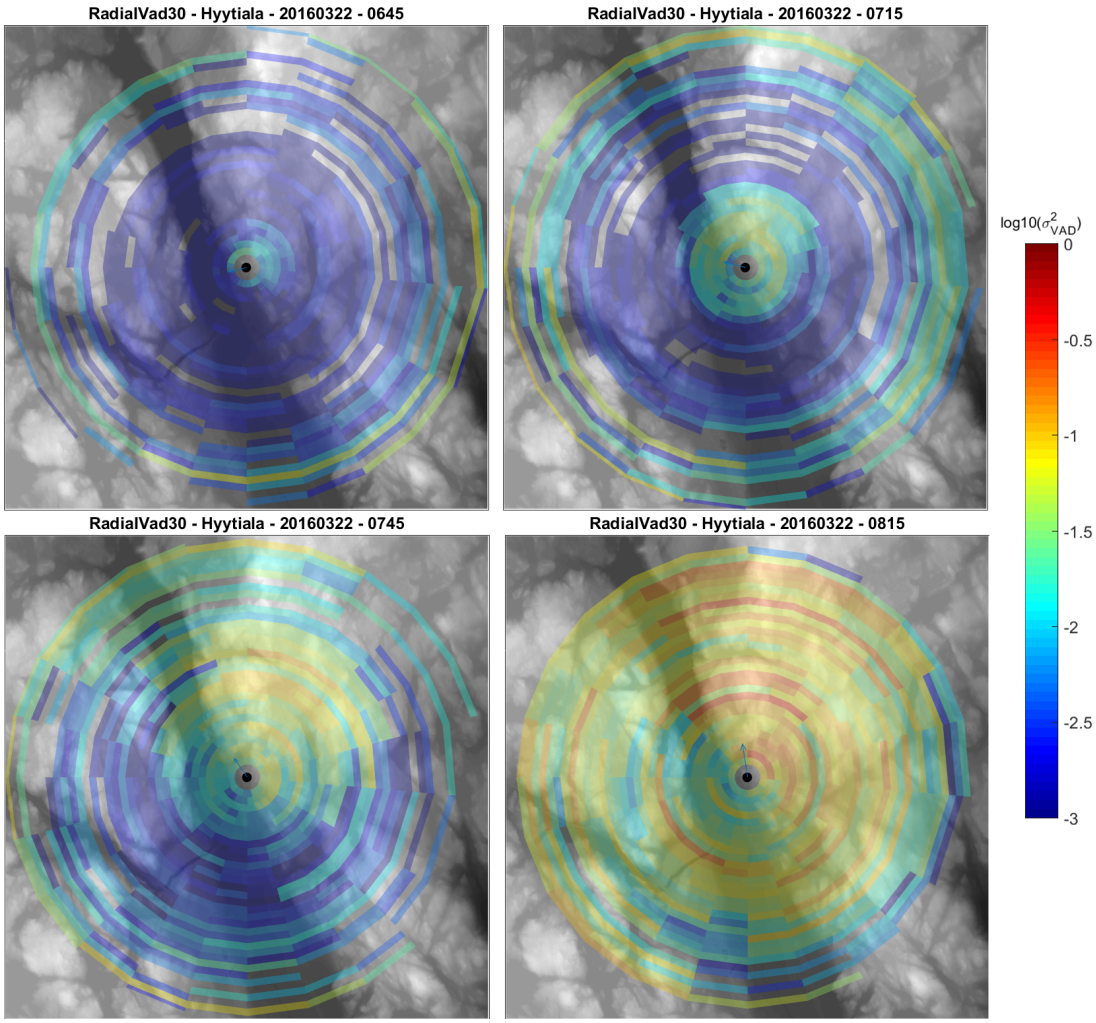

Figure 13: σ^2_{VAD} derived from Doppler lidar VAD30 scans separated into their directional components at the Hyytiälä forestry field station on 22nd March 2016. The results are presented as a color map over a grey–scale relief map of the surroundings. The Doppler lidar location is marked with the black dot in the center of the plot. North points towards the top of the page. The dark narrow strip to the west of the Doppler lidar is a lake. The blue arrows starting at the center of the map show the average wind direction and give indication of the wind speed within the lowest 1000 m of the atmosphere. The wind data was derived from the same VAD30 scan as the σ^2_{VAD}. The orthogonal distance from the Doppler lidar to the edge of the map is 2 km, which places the furthest data points to the altitude of 1 km. Data points with too high uncertainties are left blank.

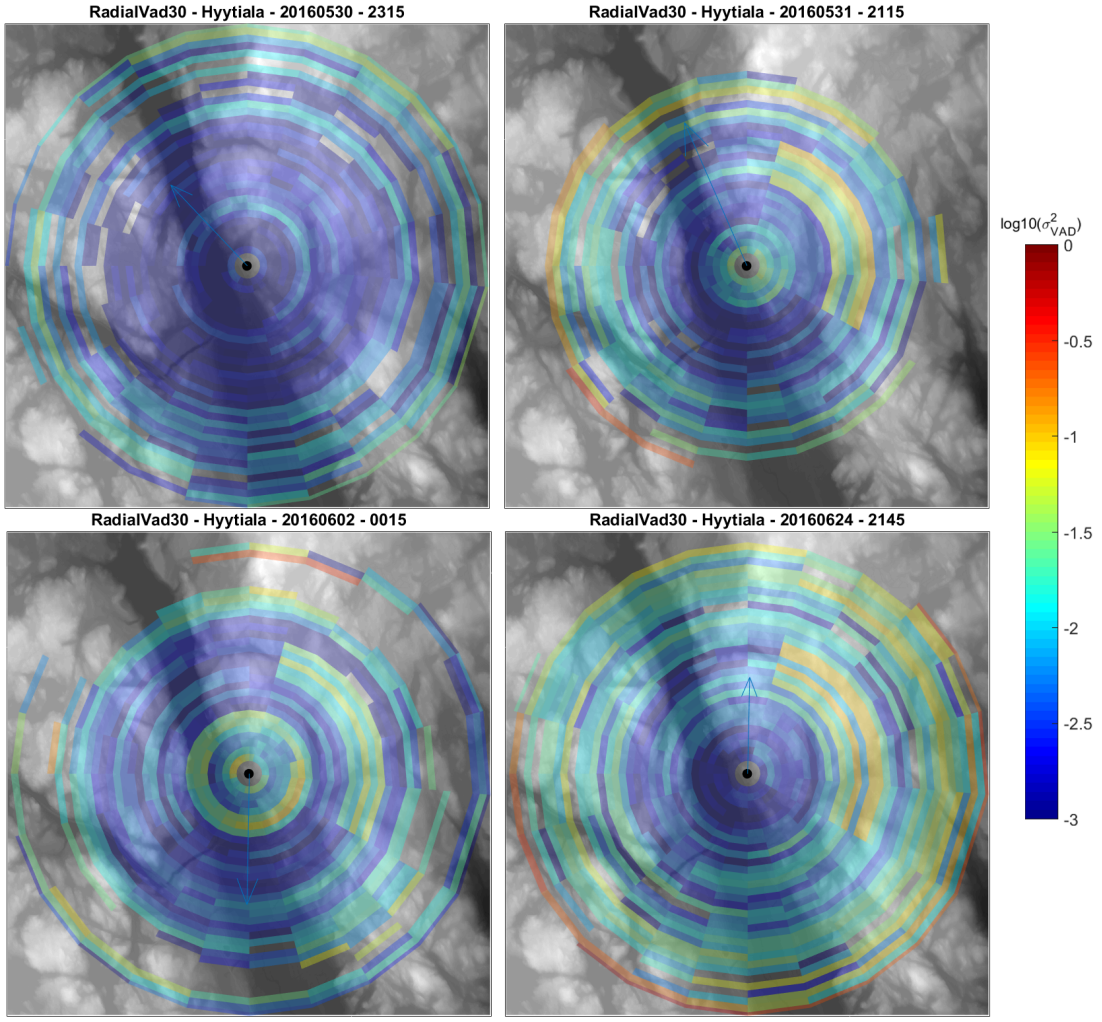

Figure 14: σ^2_{VAD} derived from Doppler lidar VAD30 scans separated into their directional components on four different nights at the Hyytiälä forestry field station. ***a)*** *30th May 2016, a calm night without spatial differences;* ***b)*** *31st May,* ***c)*** *2nd June and* ***d)*** *24th June 2016 show increased turbulence at the eastern sector. Markings are the same as those in figure 13*

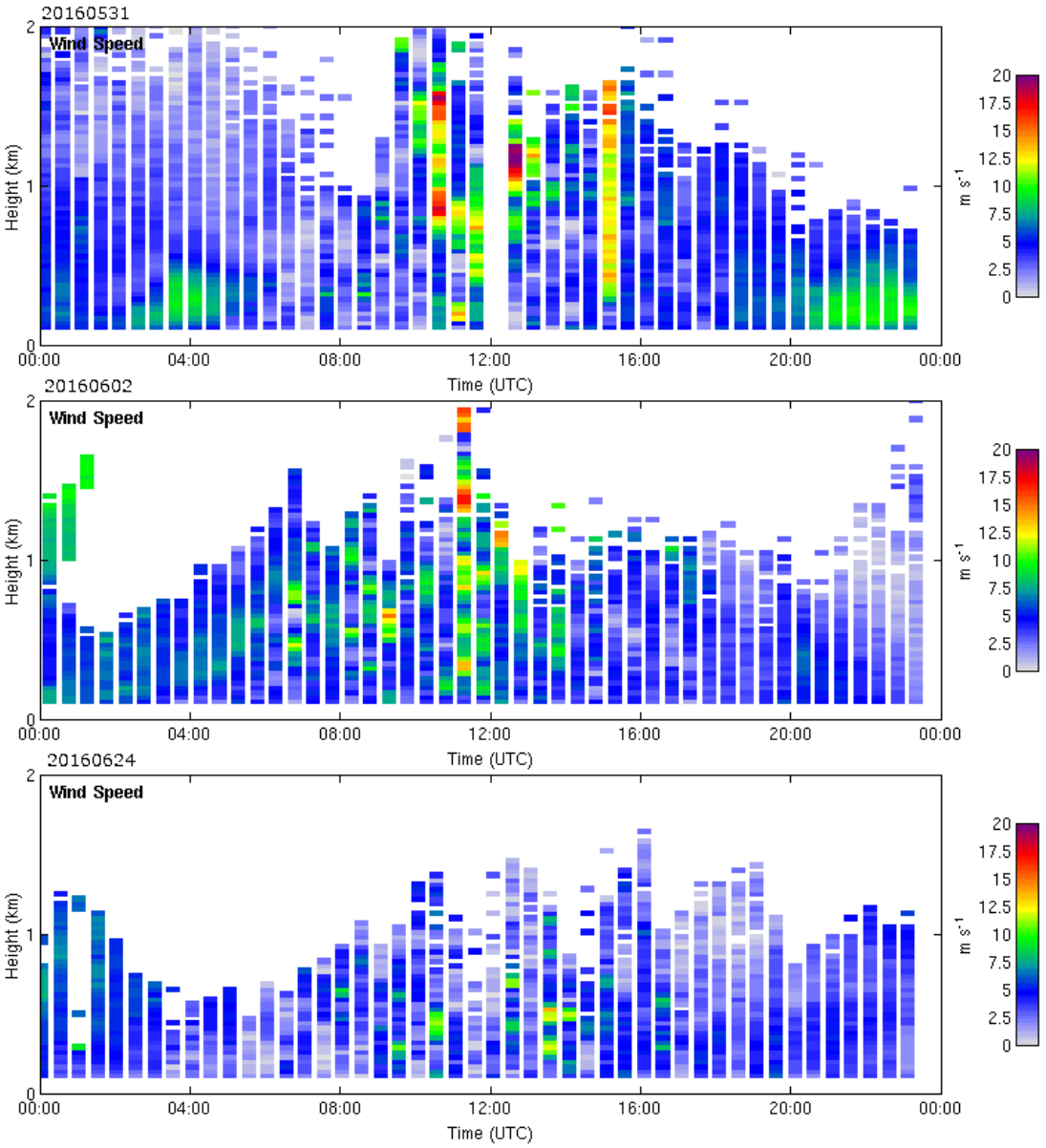

Figure 15: Horizontal wind speeds derived from Doppler lidar DBS scans at an elevation angle of 70° at the Hyytiälä forestry field station. ***a)*** *31st May,* ***b)*** *2nd June and* ***c)*** *24th June 2016.*

the turbulence field. Figures 14b, c and d show stark contrast to the calm case, with the turbulence on the eastern side of the Doppler lidar being significantly stronger than in any other direction. Comparison of the prevalent wind directions represented by the blue arrows stemming from the centres of the plots shows that no connection can be drawn between the large scale wind patterns and the turbulent structure detected. Even though the wind directions vary greatly between the plots, the most predominant region of high turbulence remains almost identical.

Further differences in the winds of the turbulent cases can be seen in figure 15, which presents the horizontal winds derived with the Doppler lidar for the cases shown in figures 14b, c and d. On 31st May (figures 14b and 15a) the horizontal wind data shows a clear nocturnal low–level jet between 20:00 and 00:00 UTC matching the 21:15 UTC time stamp of the directional σ^2_{VAD} plot. Due to the jet there will be some wind shear present that is at least partially responsible for the turbulence that was observed. While the reason for the spatial distribution of the turbulence is not certain, it is reasonable to assume that the area where more turbulence is observed is the region that is more likely to interact with the jet and experience the associated turbulence due to its higher elevation and the higher surface roughness of the canopy on the ridge compared to the surface of the lake. On 2nd June 2016 (figures 14c and 15b) the remnants of a decaying nocturnal jet are also visible. Note that the jet is travelling in a different direction to the earlier example.

On 24th June the intensity of the turbulence above the ridge (figure 14d) is stronger than in the previous cases, but the horizontal wind data (figure 15c) does not indicate any clear signs of a nocturnal jet close to the 21:45 UTC time stamp for figure 14d. Based on the datasets used in this study, no explanation for the observed turbulence could be found. Several cases resembling each of those shown in figure 14 were observed throughout the summer, leaving the subject open for further study.

The mast lies within the zone in which the higher values of directional σ^2_{VAD} were observed, and dissipation rates derived from the lower levels of the mast also indicated mixing at the same time as the Doppler lidar scans. As the mast dissipation rates are point measurements with vertical reach limited to the height of the mast, it is difficult to identify if a nocturnal jet is present from the mast measurements alone.

Although there is no certainty for the mechanism, or mechanisms, causing the local scale turbulent phenomena that was observed, the working hypothesis that they are driven by local nocturnal jets and/or surface roughness differences between the forest and the lake seem highly probable. The nocturnal turbulent mixing may have significant implications for some of the aerosol and the canopy exchange research performed in the

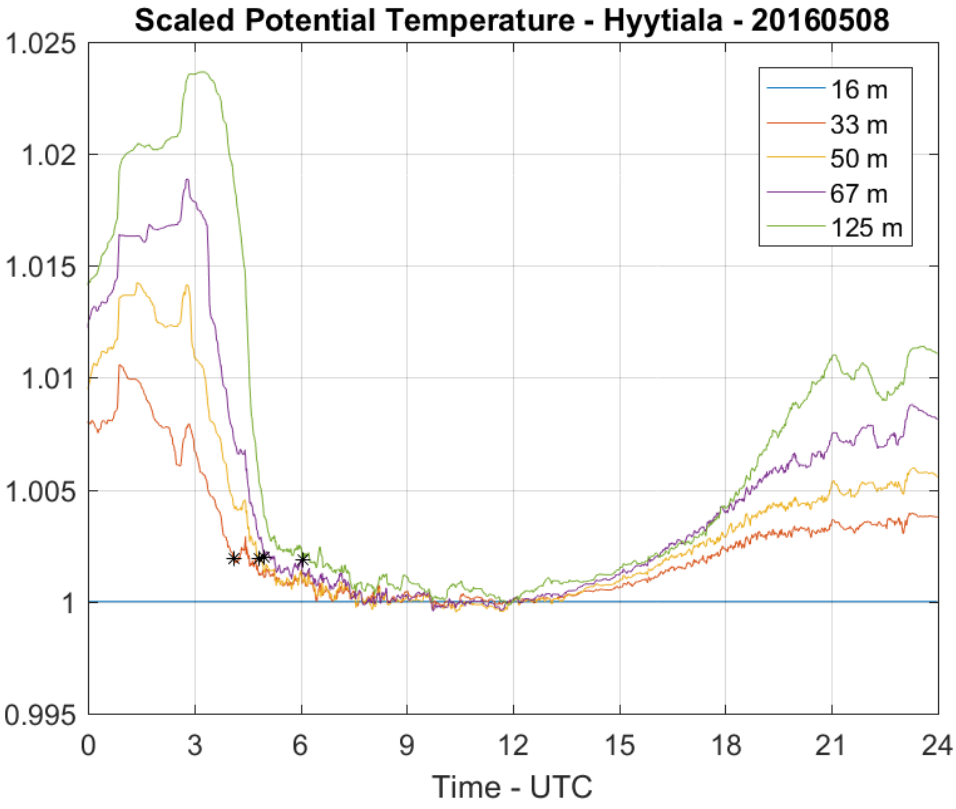

Figure 16: Time series of corrected potential temperatures from the mast at various altitudes scaled with respect to the potential temperature at 16 m at the Hyytiälä forestry field station on 8th May 2016. Atmospheric stability is near–neutral when the time series are close together, stable if the values increase with height, and unstable if the values decrease with height. The black dots represent the first instance when a particular altitude is considered to be coupled with the surface, i.e. well–mixed.

area, and thus requires further studying. More information on the 3-dimensional wind and turbulence fields are required to provide enough details to deduce unambiguously, the mechanisms causing the phenomena.

4.3 Stability

Turbulent mixing in the lowest layer of the BL was investigated using the mast data after applying the methods described in section 3.2.3 to the potential temperature time series. Although correction for the erroneous calibration of the thermometers was applied to the data sets and the results look promising, the calibration changes with

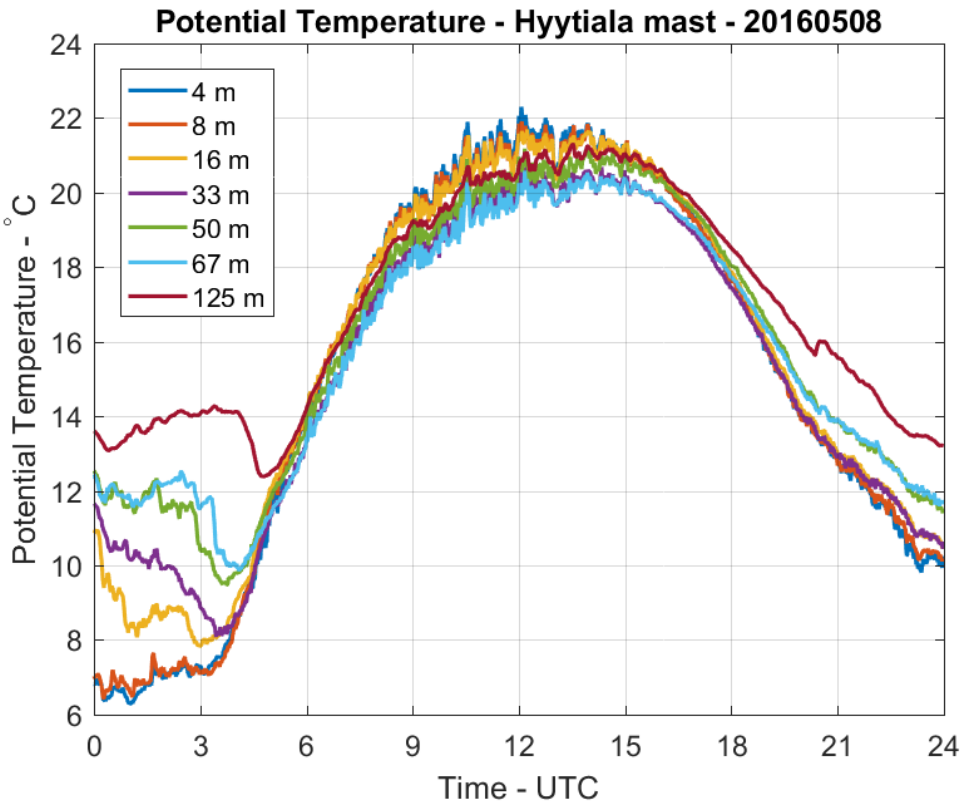

Figure 17: Potential temperatures derived from temperature measurements on the mast at various altitudes at the Hyytiälä forestry field station on 8th May 2016.

time and there may be an additional error contribution present in the data and not accounted for.

Figure 16 shows a scaled time series of corrected potential temperatures from 8th May 2016. The diurnal cycle is clear and as expected, with most of the days during autumn and spring resembling this one. The preceding night is clearly stable as the scaled values of potential temperature increase with altitude, with the larger the differences between the levels, the more stable the situation. Towards the morning, the stability decreases and finally the situation becomes neutral, indicating the presence of turbulent mixing. The time when a particular altitude became coupled with the surface (represented by the 16 m data) is indicated with a black dot, and can be used to derive the ML growth rate. The initial growth of the ML is rather slow as the layer from the surface to 33 m becomes mixed around 04:00 UTC while it takes until 06:00 UTC before the ML reaches 125 m. The time series stay tightly together until 16:00

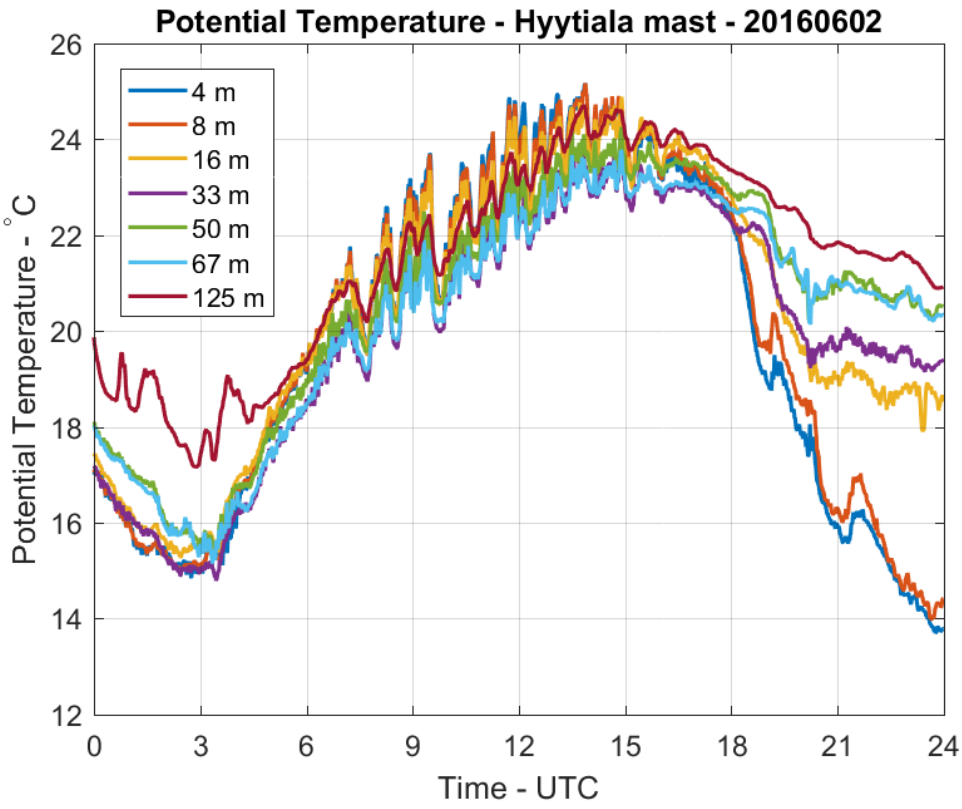

Figure 18: Potential temperatures derived from temperature measurements on the mast at various altitudes at the Hyytiälä forestry field station on 2nd June 2016.

UTC, when they begin to separate slowly as the radiative cooling from the surface at night forms a stable NBL.

The potential temperature plot from the same day shown in figure 17 indicates similar behaviour, although, because the data is not corrected and the base level keeps changing, it is much harder to derive quantitative information. The effects of the correction are most obvious and beneficial when comparing the 50 and 67 m measurements. The plot of uncorrected potential temperature indicates near neutral conditions with respect to the two heights during the following night, whereas the stability plot (corrected and scaled potential temperature) indicates that the situation is actually clearly stable as is expected.

On 2nd June 2016, the potential temperature (figure 18) was changing rapidly in response to changes in the surface heating caused by patchy cloud cover at the top of the BL. The fluctuations are also seen in the heat flux data, although much of the

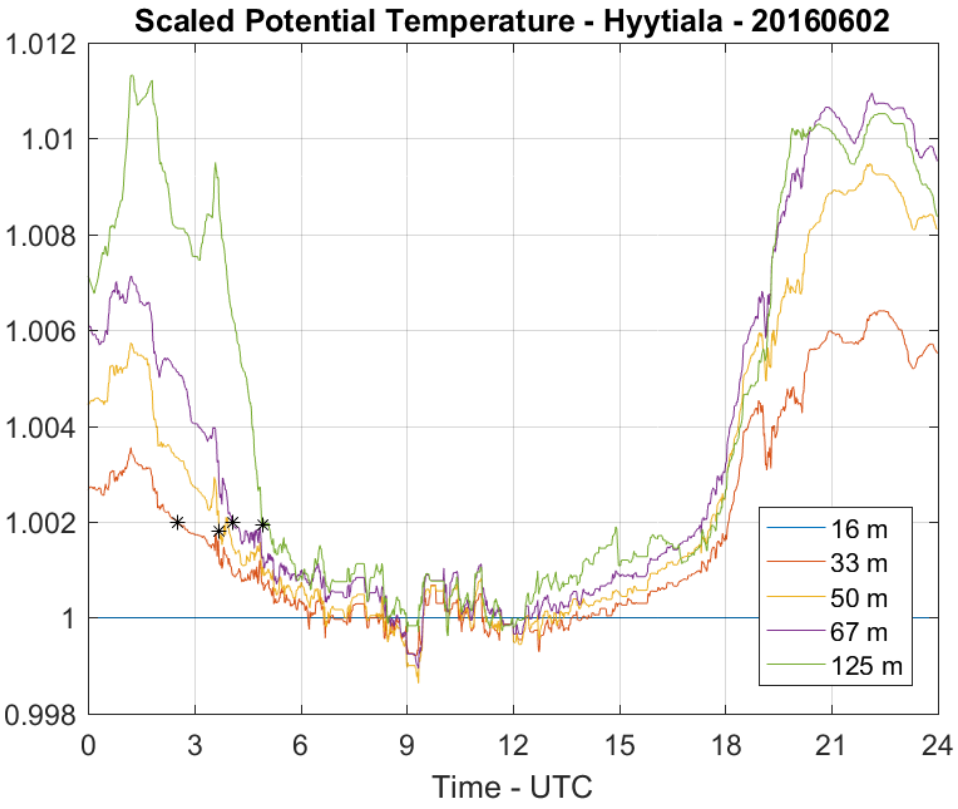

Figure 19: Time series of corrected potential temperatures from the mast at various altitudes scaled with respect to the potential temperature at 16 m at the Hyytiälä forestry field station on 2nd June 2016. Atmospheric stability is near–neutral when the time series are close together, stable if the values increase with height, and unstable if the values decrease with height. The black dots represent the first instance when a particular altitude is considered to be coupled with the surface, i.e. well–mixed.

detail is lost due to their lower temporal resolution of 30 minutes. The corrected and scaled potential temperature time series (figure 19) shows that the large fluctuations in potential temperature make very little impact on the overall stability of the lower BL. During the daytime the scaled time series from all altitudes stay closely clumped together, and only two short–lived cases of minor instability are seen. The preceding night resembles that seen on 8th May (figure 16) and the initial growth of the ML to 100 m similarly takes over 2 hours, although this initial growth occurs about an hour earlier corresponding the change in the sunrise time (from 01:49 to 00:49 UTC).

In summertime, scaled potential temperatures at the 125 m level often demonstrated unexpected behaviour in the early evening as the convection switches off and the ML

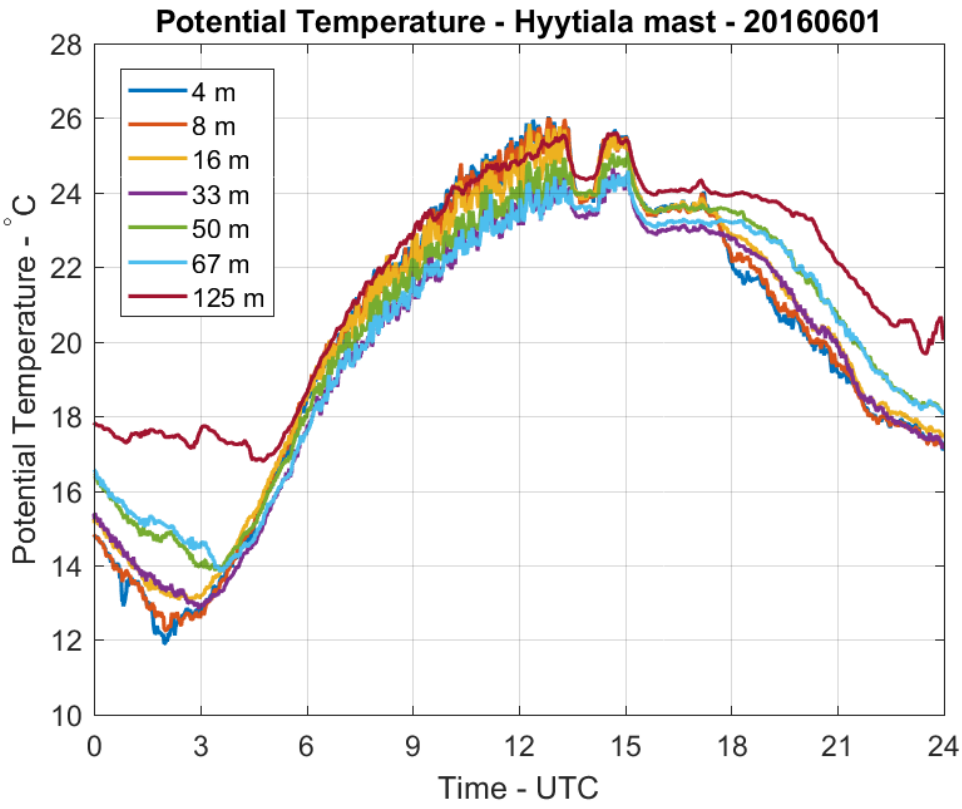

Figure 20: Potential temperatures derived from temperature measurements on the mast from various altitudes at the Hyytiälä forestry field station on 1st June 2016.

collapses and decays. In figure 19 after 16:30 UTC, 125 m scaled potential temperatures are lower than at 67 m, indicating that this layer of the atmosphere would be unstable. Some mixing is indeed seen at this level around this time in both the Doppler lidar and mast–derived turbulence data. However, because instability in the atmosphere tends to be resolved rapidly to a near neutral situation, the persistence of the unstable situation requires further study. If this phenomenon was just the result of a dynamic measurement error that was not removed in the correction process, it is not clear why it would occur only at summer.

Together with interesting behaviour seen during the collapse of the ML, other anomalies were also seen in the summer datasets. Figure 20 shows potential temperatures from 1st June 2016. A rapid drop in potential temperature is observed between 13:30-14:00 UTC resembling an almost a square–wave pattern. The change is caused by cloud cover at the top of the BL, with the heat flux also displaying a

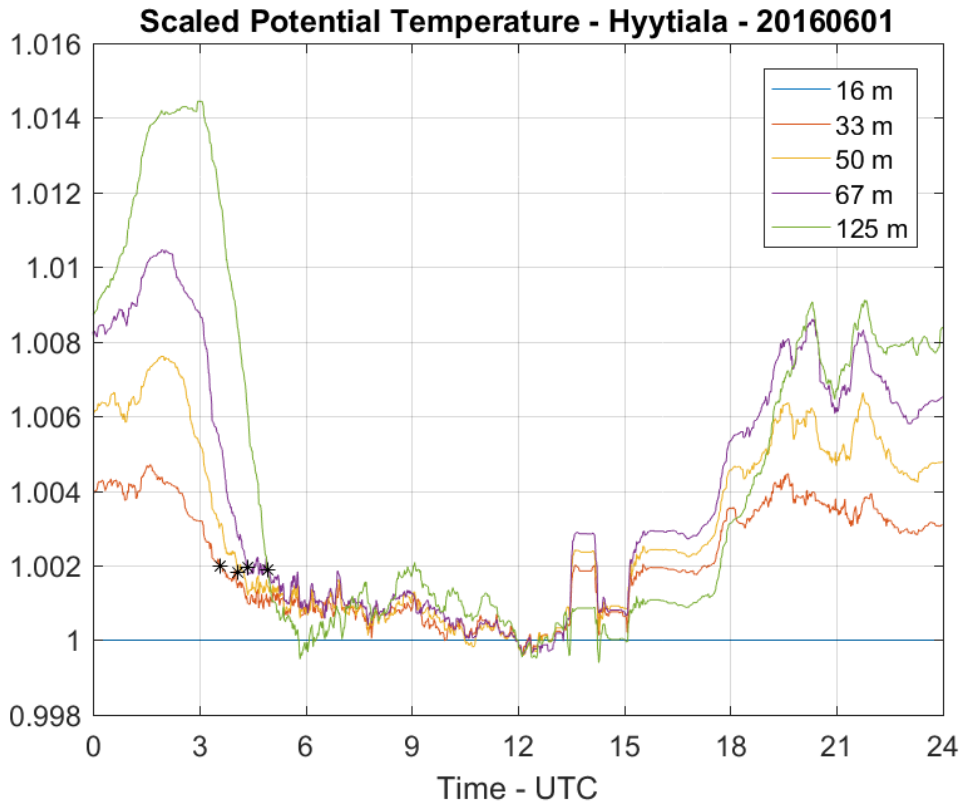

Figure 21: Time series of corrected potential temperatures from the mast at various altitudes scaled with respect to the potential temperature at 16 m at the Hyytiälä forestry field station on 1st June 2016. Atmospheric stability is near–neutral when the time series are close together, stable if the values increase with height, and unstable if the values decrease with height. The black dots represent the first instance when a particular altitude is considered to be coupled with the surface, i.e. well–mixed.

large drop around this time (not shown). The stability plot (figure 21) also shows this square–wave pattern. As was also seen in potential temperature, the reaction to the change in the surface heating was the strongest close to the surface. The magnitude of the change diminishes as it is propagated vertically through the BL creating a stable situation, with the exception of 125 m. At 125 m the reaction to the surface forcing appears greater than at 33, 50 and 67 m. As the RH was between 30-35% throughout the whole vertical span of the mast, the observation cannot be explained by differences in moisture, and may be more likely to be a result of the larger surface footprint at 125 m experiencing more heterogeneous response to the cloud.

Another anomalous situation was observed on 8th June 2016 associated with a

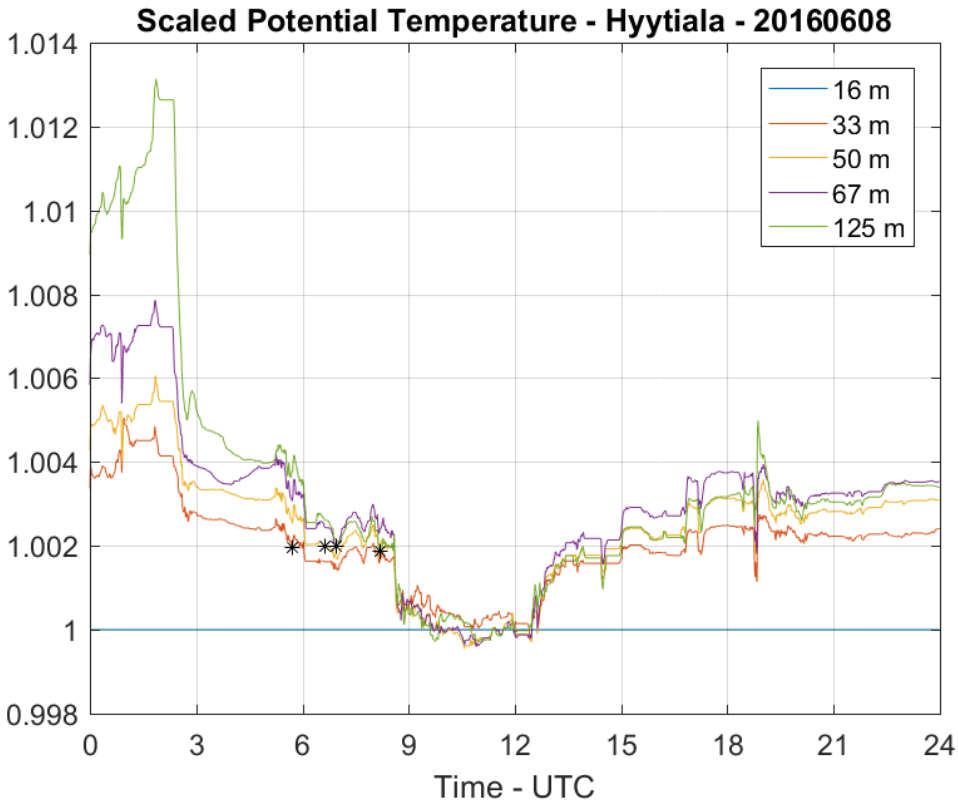

Figure 22: Time series of corrected potential temperatures from the mast at various altitudes scaled with respect to the potential temperature at 16 m at the Hyytiälä forestry field station on 8th June 2016. Atmospheric stability is near–neutral when the time series are close together, stable if the values increase with height, and unstable if the values decrease with height. The black dots represent the first instance when a particular altitude is considered to be coupled with the surface, i.e. well–mixed.

low pressure system. The whole day was characterized by strong horizontal winds ranging from $10 - 20$ m s^{-1} and all turbulent data near the surface displayed intense turbulent mixing. No coherent diurnal ML cycle was detected. The temperature time–series displayed large step changes followed by plateaus. The nature of the changes in temperature were also seen in the stability shown in figure 22. Despite the constant mixing, a transition from a stable to a neutral situation is seen during the morning hours, with the decrease in stability displaying an almost stepwise pattern. After the initial coupling of the whole layer to the top of the mast in the morning, all levels except 16 m remained clumped together (near-neutral) throughout the whole day. As the 16 m measurement level is close to the canopy, it is likely directly affected by

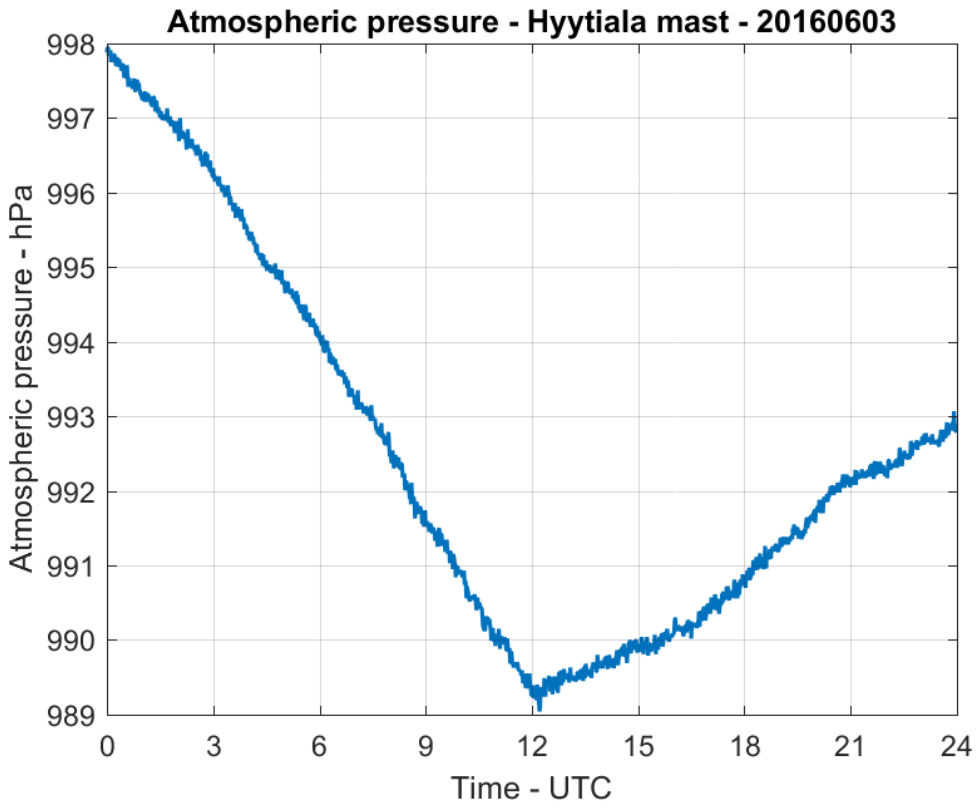

Figure 23: Ground level measurement of atmospheric pressure at the Hyytiälä forestry field station on 3rd June 2016.

mechanical friction more than the higher levels.

As these results show, the method provides promising results on characterising the stability of the lower BL and is also a useful tool for interpreting more complex meteorological situations. However the corrections that were made to the data are insufficient for quantitative analysis and for identifying minute changes in stability. The instruments need to be calibrated correctly before accurate information can be retrieved.

4.4 Case study 2

On 3rd of June 2016, a front was observed to pass over the site. The surface atmospheric pressure times series is shown in figure 23. The morning is characterized by a monotonic decrease of pressure and, just after 12:00 UTC as the front passes over, a sharp change

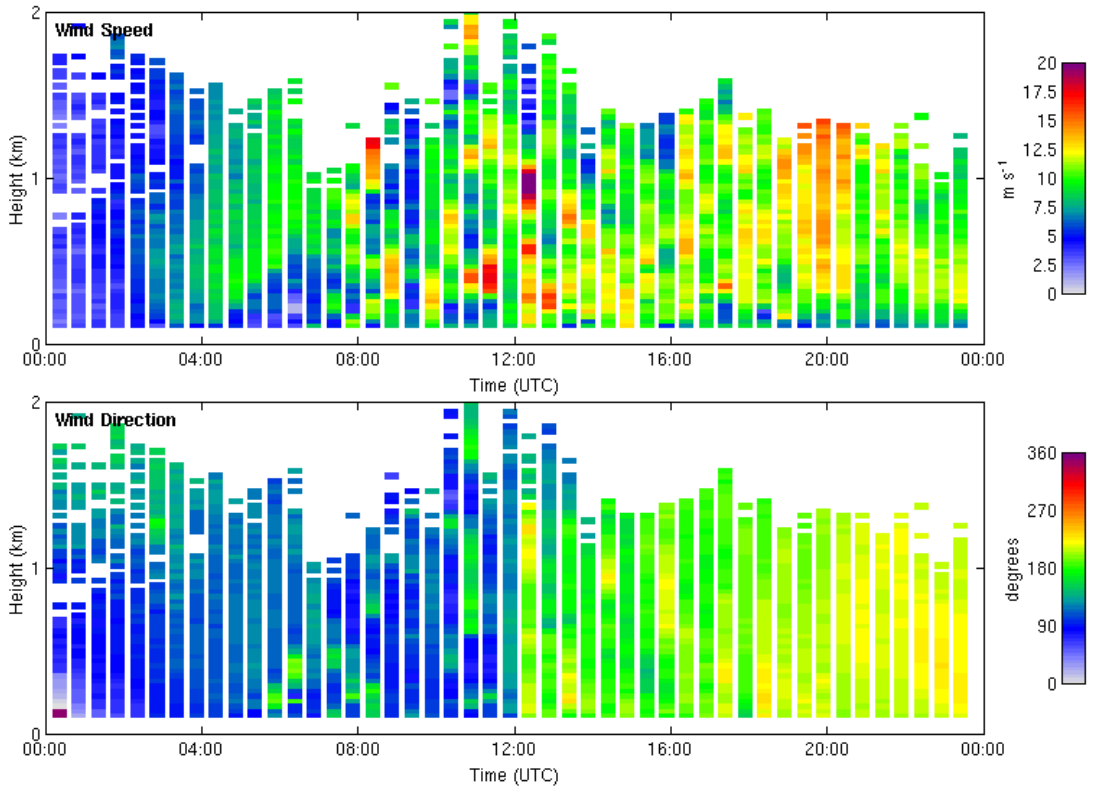

Figure 24: ***a)*** *horizontal wind speed and* ***b)*** *direction derived from Doppler lidar DBS scans at an elevation angle of 70° at the Hyytiälä forestry field station on 3rd June 2016.*

is seen after which the pressure increases monotonically. At the same time, the wind direction changes by approximately 90 ° in the Doppler lidar measurements (figure 24b). Anemometer measurements from the mast show that, near the surface, the change in wind direction happens within a few minutes. The time scale of the change aloft cannot be determined from the Doppler lidar as the scans are performed only once every half an hour. Changes in the horizontal wind speed (figure 24a) as the front passes over are not as obvious as those in the wind direction, but there is an increase in wind speed at all levels after the front has passed.

The turbulent dissipation rates derived from the Doppler lidar and the anemometer data are presented in figure 25. From 04:30 UTC onwards until 13:00 UTC, development of a canonical deep CBL can be observed. Between 13:00 and 13:30 UTC the MLH decreases rapidly, from 2000 to 1200 m. The decrease is associated with the passing

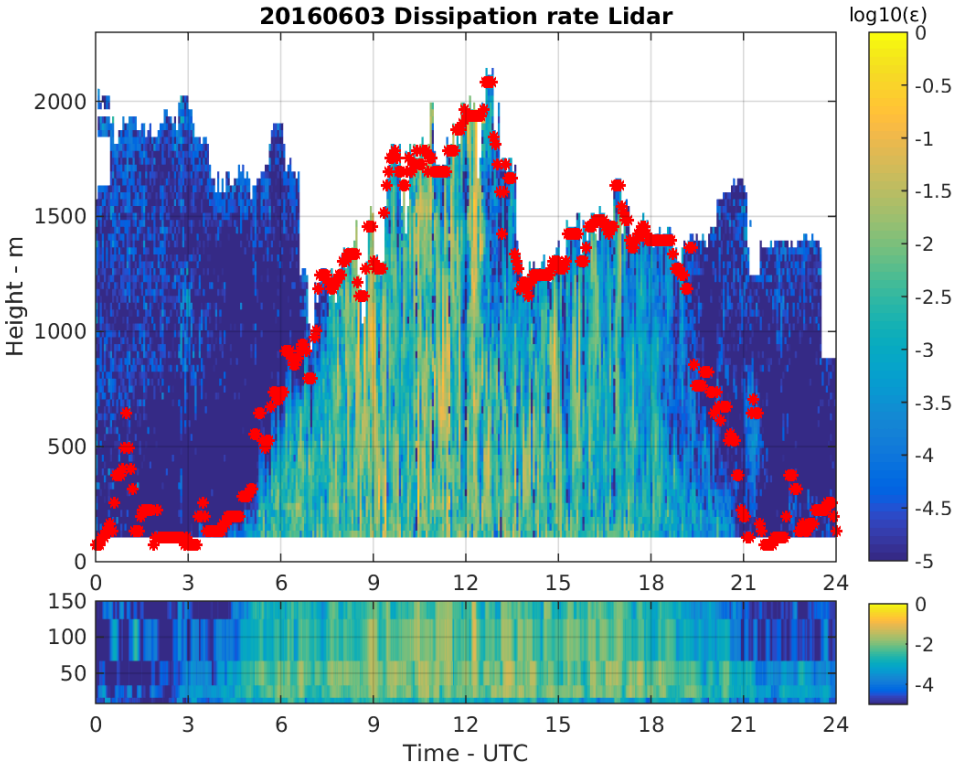

Figure 25: Dissipation rates from vertical velocity data measured by the Doppler lidar (above) and from horizontal wind measurements on the mast (below) at the Hyytiälä forestry field station on 3rd June 2016. Both plots use the same log_{10} colour scale. The red dots represent MLH derived by the algorithm described in section 3.1.5.

of the front as the preceding deep ML was replaced by a shallower one in the new air mass behind. Comparison with the in-situ measurements from the mast show that the response of the upper region of the ML is about an hour behind the surface forcings, just within the BL definition given by Stull (1988). The ML then began to grow again and the height of the new ML peaked at 1500 m around 17:00 and UTC, finally collapsing between 19:00 and 21:00 UTC.

The heat fluxes, shown in figure 26, behave as expected during the morning hours with a gradual increase to around 200 W m^{-2}. At 12:00 UTC rapid changes in both fluxes are seen as the sensible heat flux increases to above 400 W m^{-2} while the latent heat flux decreases to -400 W m^{-2}. As the temporal resolution of the fluxes is 30 minutes, much detail is left out as the changes that occurred were very rapid. At the follow-

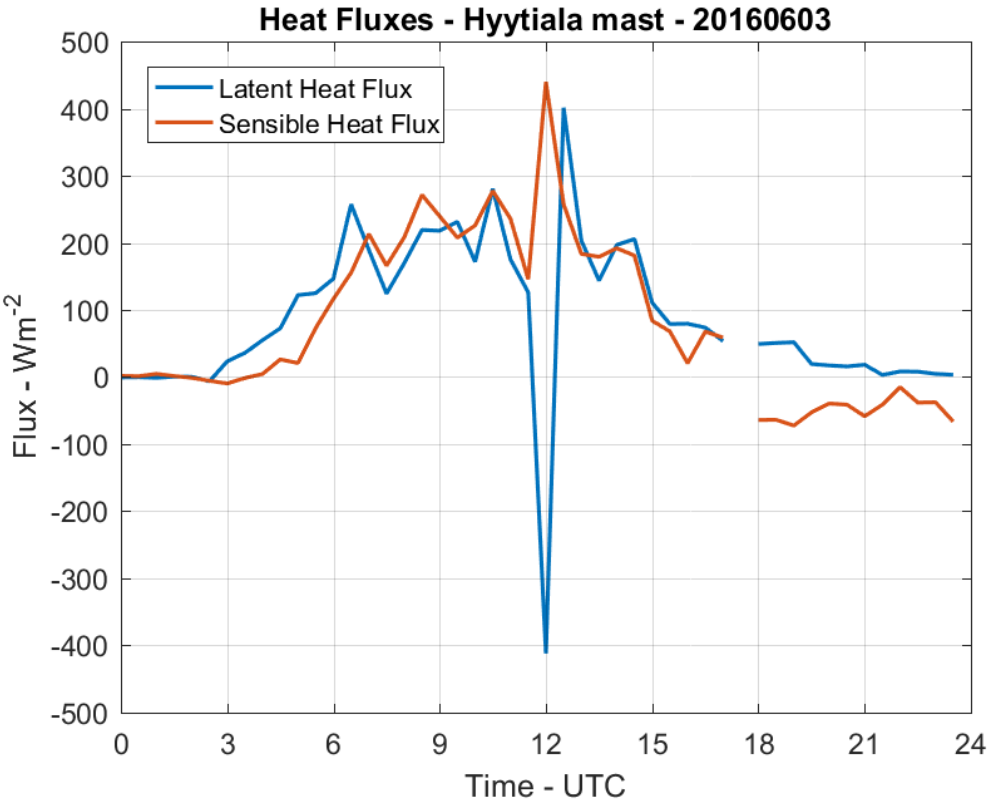

Figure 26: Heat fluxes measured on the mast 23 m above the ground at the Hyytiälä forestry field station on 3rd June 2016.

ing time stamp at 12:30 UTC the latent heat flux rapidly increases again to 400 W m^{-2}, while the sensible heat flux has already begun to stabilize around 200 W m^{-2} and by 13:00 UTC the effects of the front are no longer any more distinguishable in either flux measurement. There was not enough cloud cover to impact the surface heating dramatically as the front passed over (see figure 27), so the observed changes in various measurements can be directly attributed to changes in the air masses ahead and behind the front.

The potential temperature time series from the mast are shown in figure 28. The growth of the ML in the morning hours is clearly visible as the vertical profile changes from stable to well–mixed up to 125 m above ground between 03:00 and 05:00 UTC. At 12:00 UTC all potential temperatures increase rapidly by almost 2 $°C$ and then decrease to slightly below their values between 09:00 and 12:00 UTC. This rapid change coincides with the spikes in the flux data (and the change in pressure and wind direction). After

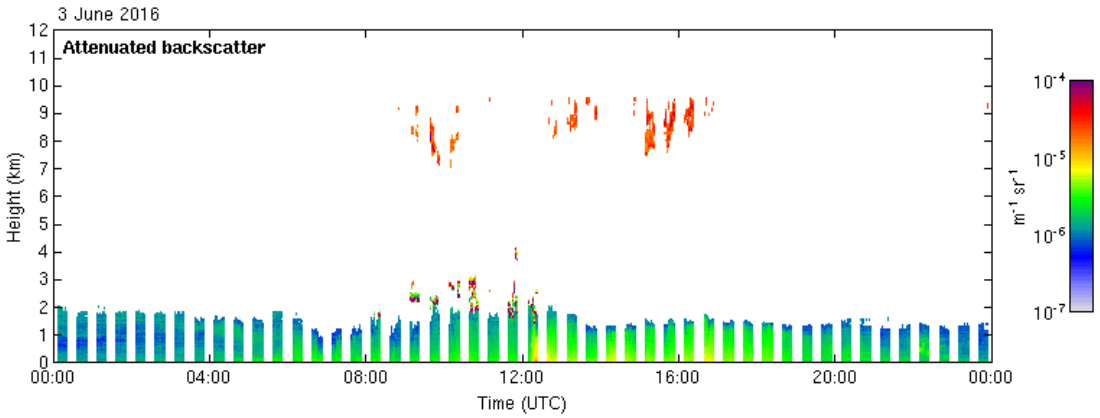

Figure 27: Attenuated backscatter measured by the Doppler lidar at the Hyytiälä forestry field station on 3rd June 2016.

the front has passed, the potential temperatures keep decreasing to values below those of the early morning. After 18:00 UTC, the potential temperatures at most heights start to diverge, indicating that the atmospheric stability is turning from well–mixed to stable, at least at the upper levels (67 and 125 m). The lower levels seem to remain well–mixed, and the anemometer data (figure 25) indicates the presence of quite strong low–level turbulence throughout the evening and night. This is shear–driven turbulence arising from the strong vertical gradient in wind speed near the surface because of the strong winds aloft.

Similar changes in atmospheric stability can also be seen in the time series of RH, shown in figure 29. After 05:00 UTC, when all potential temperature and Doppler lidar measurements indicate that the situation has become well–mixed, RH values are very similar and track each other until the evening, around 18:00 UTC. As expected, RH decreases as the temperature increases. At 12:00 UTC there is a very rapid decrease and increase in RH at all heights, which is at least partially related to the changes in temperature. RH did not remain elevated for long. The new air mass behind the front was much dryer and RH remained under 30% until the temperature dropped and the lower atmosphere started to become stable.

The passing of the front also affects the properties of the ambient aerosols. In figure 27 the attenuated backscatter from the Doppler lidar is shown. After 12:00 UTC coinciding with the increase in RH, a significant increase in the attenuated backscatter can be observed, especially near the surface. This increase is most likely a result of aerosol growth as they intake more water under the moister conditions. The effect was rather

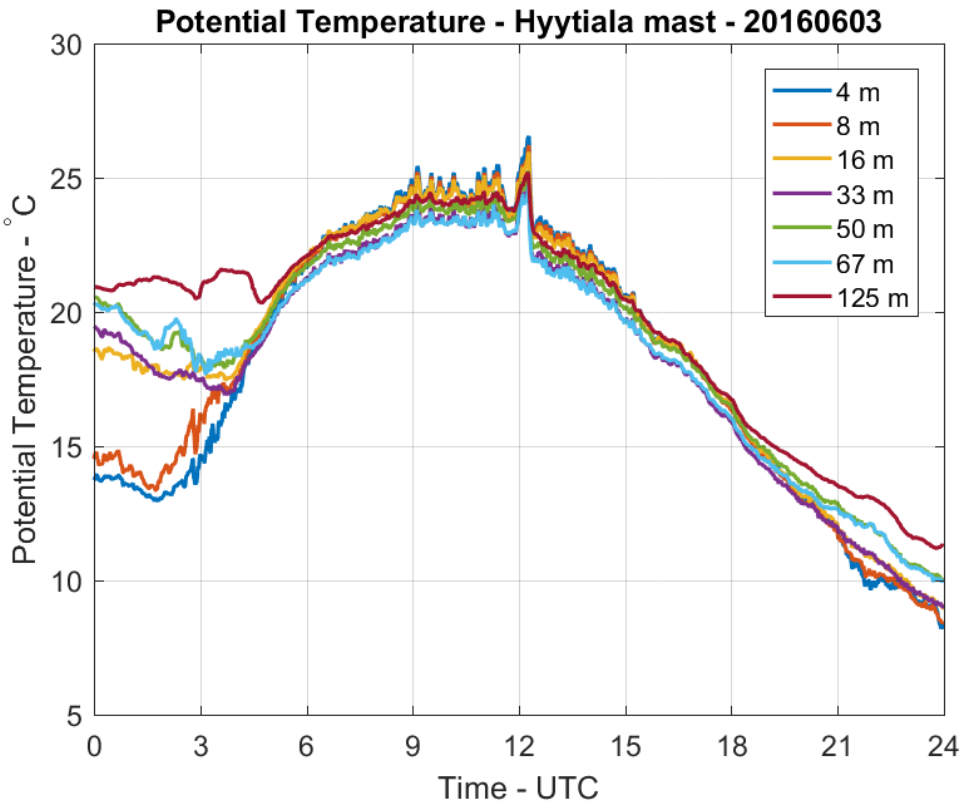

Figure 28: Potential temperatures derived from temperature measurements made on the mast at various altitudes at the Hyytiälä forestry field station on 3rd June 2016.

short–lived just as the spike in RH was. Although the attenuated backscatter seems to be slightly higher after the front has passed than before it, this may be due to a different aerosol size distribution and aerosol type in the new air mass, or less dilution and higher concentrations due to a shallower ML. In–situ aerosol measurements (available from the SMEAR station) should be investigated to determine which is responsible.

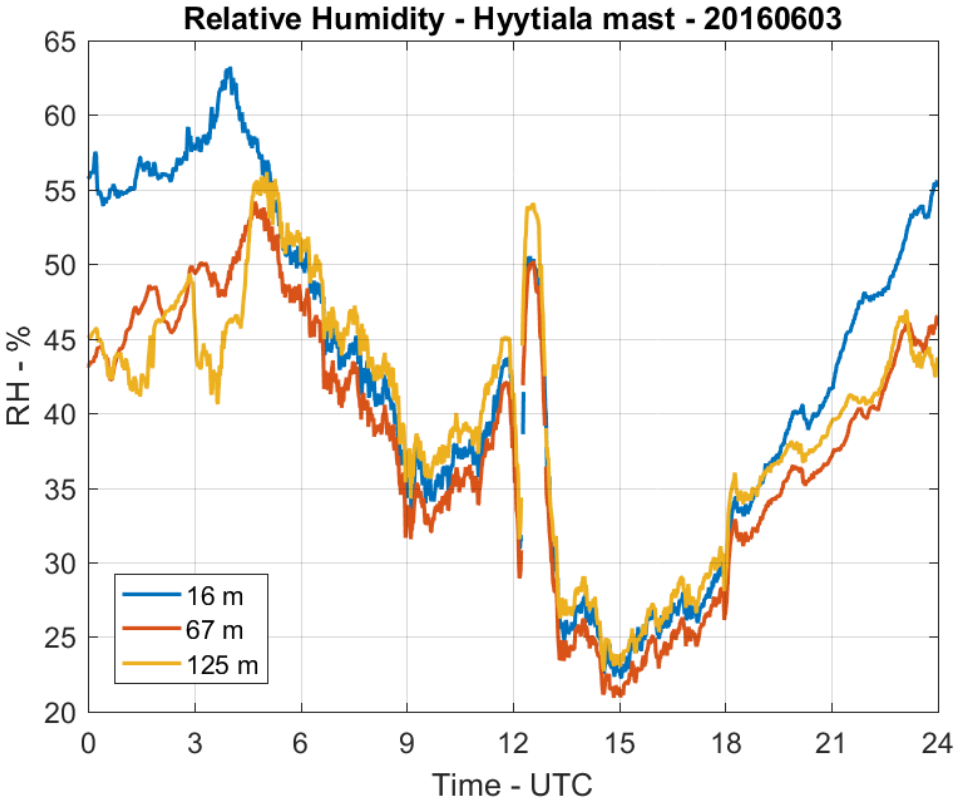

Figure 29: Relative humidities measured on mast at various altitudes at the Hyytiälä forestry field station on 3rd June 2016.

5 Conclusions

The results of this study show how combining turbulent data from Doppler lidar vertical staring mode and VAD scans with in–situ measurements from a mast provides a more complete picture of the mixing processes in the BL. This allows a more accurate assessment of the observed phenomena and how they may impact other areas of research. Including other meteorological factors in the analysis helps to clarify situations with more complex mixing patterns, such as those seen associated with frontal systems or nocturnal jets. One of the case studies presented strongly suggests a causal relationship between sudden changes in heat fluxes and the initiation of a nocturnal jet.

New developments in two complementary methods showed promising results and they were capable of detecting phenomena which would be difficult to identify in standard datasets. Scaled potential temperature profiles from the mast show how the profile of atmospheric stability responds to changes in surface heating. Separating turbulent properties derived from a Doppler lidar VAD scan into its directional components shows that ML growth can be spatially heterogeneous and that at the Hyytiälä forestry field station stark spatial differences in turbulence occur rather frequently during summer nights. The most intense nocturnal turbulence usually occurs close to the SMEAR–II station and may need to be accounted for when drawing certain conclusions from the aerosol and flux research performed here. The mechanism behind this mixing is not yet clear, but seems to be connected to nocturnal jets and spatial differences in surface roughness. Implications of this phenomenon require further studying.

Calculating potential temperature from the mast measurements indicated issues in the calibration of the thermometers on the mast. Systematic differences were observed in the values measured by different thermometers during well mixed conditions (corroborated by the Doppler lidar data) when the potential temperature profile should be constant. A constant offset correction for each daily profile was necessary so that the profile of atmospheric stability could be studied. This correction was sufficient for the autumn and spring datasets, but for more accurate and quantitative data analysis (especially during the summertime when the most ambiguous behaviour was observed), calibration of the thermometers is necessary. This method of generating potential temperature profiles is a novel means of detecting thermometer calibration issues in mast datasets.

References

W. M. Angevine, A. W. Grimsdell, L. M. Hartten, and A. C. Delany. The Flatland boundary layer experiments. *Bulletin of the American Meteorological Society*, 79(3): 419–431, 1998. doi: 10.1175/1520-0477(1998)079<0419:TFBLE>2.0.CO;2.

J. Bange, T. Spieß, and A. van den Kroonenberg. Characteristics of the early-morning shallow convective boundary layer from Helipod flights during STINHO-2. *Theoretical and Applied Climatology*, 90(1-2):113, 2007. ISSN 1434-4483. doi: 10.1007/s00704-006-0272-2.

F. Beyrich and U. Görsdorf. Composing the diurnal cycle of mixing height from simultaneous sodar and wind profiler measurements. *Boundary-Layer Meteorology*, 76(4): 387–394, 1995. ISSN 1573-1472. doi: 10.1007/BF00709240.

J. A. Businger, J. C. Wyngaard, Y. Izumi, and E. F. Bradley. Flux-profile relationships in the atmospheric surface layer. *Journal of the Atmospheric Sciences*, 28(2):181–189, 1971. doi: 10.1175/1520-0469(1971)028<0181:FPRITA>2.0.CO;2.

S. Casadio, A. Di Sarra, G. Fiocco, D. Fuà, F. Lena, and M. P. Rao. Convective characteristics of the nocturnal urban boundary layer as observed with Doppler sodar and Raman lidar. *Boundary-Layer Meteorology*, 79(4):375–391, 1996. doi: 10.1007/BF00119405.

N. L. Dias, J. E. Gonçalves, L. S. Freire, T. Hasegawa, and A. L. Malheiros. Obtaining potential virtual temperature profiles, entrainment fluxes, and spectra from mini unmanned aerial vehicle data. *Boundary-Layer Meteorology*, 145(1):93–111, 2012. ISSN 1573-1472. doi: 10.1007/s10546-011-9693-2.

F. Dominici, R. D. Peng, M. L. Bell, L. Pham, A. McDermott, S. L. Zeger, and J. M. Samet. Fine particulate air pollution and hospital admission for cardiovascular and respiratory diseases. *Journal of the American Medical Association*, 295(10):1127–1134, 2006. doi: 10.1001/jama.295.10.1127.

W. L. Golding. Low-level windshear and its impact on airlines. *Journal of Aviation/Aerospace Education & Research*, 14(2), 2005.

P. Hari and M. Kulmala. Station for Measuring EcosystemAtmosphere Relations (SMEAR II). *Boreal Env. Res.*, 2005.

A. Hirsikko, E. J. O'Connor, M. Komppula, K. Korhonen, A. Pfüller, E. Giannakaki, C. R. Wood, M. Bauer-Pfundstein, A. Poikonen, T. Karppinen, H. Lonka, M. Kurri, J. Heinonen, D. Moisseev, E. Asmi, V. Aaltonen, A. Nordbo, E. Rodriguez, H. Lihavainen, A. Laaksonen, K. E. J. Lehtinen, T. Laurila, T. Petäjä, M. Kulmala, and Y. Viisanen. Observing wind, aerosol particles, cloud and precipitation: Finland's new ground-based remote-sensing network. *Atmos. Meas. Tech.*, 7(5):1351–1375, 2014. doi: 10.5194/amt-7-1351-2014.

D. Y. Hollinger, F. M. Kelliher, J. N. Byers, J. E. Hunt, T. M. McSeveny, and P. L. Weir. Carbon dioxide exchange between an undisturbed old-growth temperate forest and the atmosphere. *Ecology*, 75(1):134–150, 1994. ISSN 1939-9170. doi: 10.2307/1939390.

A. Ibald-Mulli, H.-E. Wichmann, W. Kreyling, and A. Peters. Epidemiological evidence on health effects of ultrafine particles. *Journal of Aerosol Medicine*, 15:189–201, 2002. doi: doi: 10.1089/089426802320282310.

A. D. Kappos, P. Bruckmann, T. Eikmann, N. Englert, U. Heinrich, P. Höppe, E. Koch, G. H. M. Krause, W. G. Kreyling, K. Rauchfuss, P. Rombout, V. Schulz-Klemp, W. R. Thiel, and H.-E. Wichmann. Health effects of particles in ambient air. *International Journal of Hygiene and Environmental Health*, 207(4):399 – 407, 2004. ISSN 1438-4639. doi: http://dx.doi.org/10.1078/1438-4639-00306.

D. Khelif, S. P. Burns, and C. A. Friehe. Improved wind measurements on research aircraft. *Journal of Atmospheric and Oceanic Technology*, 16(7):860–875, 1999. doi: 10.1175/1520-0426(1999)016<0860:IWMORA>2.0.CO;2.

M. Kossmann and A. Sturman. The surface wind field during winter smog nights in Christchurch and coastal Canterbury, New Zealand. *International Journal of Climatology*, 24(1):93–108, 2004. ISSN 1097-0088. doi: 10.1002/joc.981.

M. Kulmala, K. Hämeri, P. P. Aalto, J. M. Mäkelä, L. Pirjola, E. DOouglas Nilsson, G. Buzorius, . Rannik, M. Dal Maso, W. Seidl, T. Hoffman, R. Janson, H.-C. Hansson, Y. Viisanen, A. Laaksonen, and C. D. O'Dowd. Overview of the international project on biogenic aerosol formation in the boreal forest (BIOFOR). *Tellus B*, 53 (4):324–343, 2001. ISSN 1600-0889. doi: 10.1034/j.1600-0889.2001.530402.x.

S.E. Lane, J.F. Barlow, and C.R. Wood. An assessment of a three-beam Doppler lidar wind profiling method for use in urban areas. *Journal of Wind Engi-*

neering and Industrial Aerodynamics, 119:53 – 59, 2013. ISSN 0167-6105. doi: https://doi.org/10.1016/j.jweia.2013.05.010.

W. G. Large and S. Pond. Sensible and latent heat flux measurements over the ocean. *Journal of Physical Oceanography*, 12(5):464–482, 1982. doi: 10.1175/1520-0485(1982)012<0464:SALHFM>2.0.CO;2.

A. Lemonsu, So. Bastin, V. Masson, and P. Drobinski. Vertical structure of the urban boundary layer over Marseille under sea-breeze conditions. *Boundary-Layer Meteorology*, 118(3):477–501, 2006. ISSN 1573-1472. doi: 10.1007/s10546-005-7772-y.

A. J. Manninen, E. J. O'Connor, V. Vakkari, and T. Petäjä. A generalised background correction algorithm for a Halo Doppler lidar and its application to data from Finland. *Atmospheric Measurement Techniques*, 9(2):817–827, 2016. doi: 10.5194/amt-9-817-2016.

S. Martin, F. Beyrich, and J. Bange. Observing entrainment processes using a small unmanned aerial vehicle: A feasibility study. *Boundary-Layer Meteorology*, 150(3): 449–467, 2014. ISSN 1573-1472. doi: 10.1007/s10546-013-9880-4.

J. A. McKay. Modeling of direct detection Doppler wind lidar. I. The edge technique. *Appl. Opt.*, 37(27):6480–6486, Sep 1998. doi: 10.1364/AO.37.006480.

R. T. Menzies and R. M. Hardesty. Coherent Doppler lidar for measurements of wind fields. *Proceedings of the IEEE*, 77(3):449–462, Mar 1989. ISSN 0018-9219. doi: 10.1109/5.24130.

E. D. Nilsson, Ü. Rannik, M. Kulmala, G. Buzorius, and C. D. O'Dowd. Effects of continental boundary layer evolution, convection, turbulence and entrainment, on aerosol formation. *Tellus B*, 53(4):441–461, 2001. ISSN 1600-0889. doi: 10.1034/j.1600-0889.2001.530409.x.

E. J. O'Connor, A. J. Illingworth, I. M. Brooks, C. D. Westbrook, R. J. Hogan, F. Davies, and B. J. Brooks. A method for estimating the turbulent kinetic energy dissipation rate from a vertically pointing Doppler lidar, and independent evaluation from balloon-borne in situ measurements. *Journal of Atmospheric and Oceanic Technology*, 27(10):1652–1664, 2010. doi: 10.1175/2010JTECHA1455.1.

E. Päschke, R. Leinweber, and V. Lehmann. An assessment of the performance of a 1.5 μm Doppler lidar for operational vertical wind profiling based on a 1-year trial.

Atmospheric Measurement Techniques, 8(6):2251–2266, 2015. doi: 10.5194/amt-8-2251-2015.

G. Pearson, F. Davies, and C. Collier. An analysis of the performance of the UFAM pulsed Doppler lidar for observing the boundary layer. *Journal of Atmospheric and Oceanic Technology*, 26(240-250), 2009.

T. Petäjä, E. J. O'Connor, D. Moisseev, V. A. Sinclair, A. J. Manninen, R. Väänänen, A. von Lerber, J. A. Thornton, K. Nicoll, W. Petersen, V. Chandrasekar, J. N. Smith, . M. Winkler, O. Krüger, H. Hakola, H. Timonen, D. Brus, T. Laurila, E. Asmi, M. Riekkola, L. Mona, P. Massoli, R. Engelmann, M. Komppula, J. Wang, C. Kuang, J. Bäck, A. Virtanen, J. Levula, M. Ritsche, and N. Hickmon. BAECC: A field campaign to elucidate the impact of biogenic aerosols on clouds and climate. *Bulletin of the American Meteorological Society*, 97(10):1909–1928, 2016. doi: 10.1175/BAMS-D-14-00199.1.

C. A. Pope, R. T. Burnett, M. J. Thun, E. E. Calle, D. Krewski, K. Ito, and G. D. Thurston. Lung cancer, cardiopulmonary mortality, and long-term exposure to fine particulate air pollution. *Journal of the American Medical Association*, 287(9):1132–1141, 2002. doi: 10.1001/jama.287.9.1132.

B. Rappenglück, P. Oyola, I. Olaeta, and P. Fabian. The evolution of photochemical smog in the metropolitan area of Santiago de Chile. *Journal of Applied Meteorology*, 39(3):275–290, 2000. doi: 10.1175/1520-0450(2000)039<0275:TEOPSI>2.0.CO;2.

C. Rebmann, O. Kolle, B. Heinesch, R. Queck, A. Ibrom, and M. Aubinet. *Data Acquisition and Flux Calculations*, pages 59–84. Springer, 2012. ISBN 978-94-007-2350-4. doi: 10.1007/978-94-007-2351-1-3.

O. Reitebuch. *Wind Lidar for Atmospheric Research*, pages 487–507. Springer Berlin Heidelberg, Berlin, Heidelberg, 2012. ISBN 978-3-642-30183-4. doi: 10.1007/978-3-642-30183-4-30.

B. J. Rye. Antenna parameters for incoherent backscatter heterodyne lidar. *Appl. Opt.*, 18(9):1390–1398, May 1979. doi: 10.1364/AO.18.001390.

B. J. Rye and R. M. Hardesty. Discrete spectral peak estimation in incoherent backscatter heterodyne lidar. I. Spectral accumulation and the Cramer-Rao lower bound. *IEEE Transactions on Geoscience and Remote Sensing*, 31(1):16–27, Jan 1993. ISSN 0196-2892. doi: 10.1109/36.210440.

K. Schäfer, S. Emeis, H. Hoffmann, and C. Jahn. Influence of mixing layer height upon air pollution in urban and sub-urban areas. *Meteorologische Zeitschrift*, 15(6): 647–658, 12 2006. doi: 10.1127/0941-2948/2006/0164.

J. H. Schween, A. Hirsikko, U. Löhnert, and S. Crewell. Mixing-layer height retrieval with ceilometer and Doppler lidar: from case studies to long-term assessment. *Atmospheric Measurement Techniques*, 7(11):3685–3704, 2014. doi: 10.5194/amt-7-3685-2014.

P. Seibert, F. Beyrich, S.-E. Gryning, S. Joffre, A. Rasmussen, and P. Tercier. Review and intercomparison of operational methods for the determination of the mixing height. *Atmospheric Environment*, 34:1001–1027, 2000. ISSN 1352-2310. doi: 10.1016/S1352-2310(99)00349-0.

H. Siebert, M. Wendisch, T. Conrath, U. Teichmann, and J. Heintzenberg. A new tethered balloon-borne payload for fine-scale observations in the cloudy boundary layer. *Boundary-Layer Meteorology*, 106(3):461–482, 2003. ISSN 1573-1472. doi: 10.1023/A:1021242305810.

R.B. Stull. *An Introduction to Boundary Layer Meteorology*. Atmospheric and Oceanographic Sciences Library. Springer Netherlands, 1988. ISBN 9789027727695. doi: 10.1007/978-94-009-3027-8.

K. Träumner, Ch. Kottmeier, U. Corsmeier, and A. Wieser. Convective boundary-layer entrainment: Short review and progress using Doppler lidar. *Boundary-Layer Meteorology*, 141(3):369–391, 2011. ISSN 1573-1472. doi: 10.1007/s10546-011-9657-6.

S. C. Tucker, C. J. Senff, A. M. Weickmann, W. A. Brewer, R. M. Banta, S. P. Sandberg, D. C. Law, and R. M. Hardesty. Doppler lidar estimation of mixing height using turbulence, shear, and aerosol profiles. *Journal of Atmospheric and Oceanic Technology*, 26(4):673–688, 2009. doi: 10.1175/2008JTECHA1157.1.

V. Vakkari, E. J. O'Connor, A. Nisantzi, R. E. Mamouri, and D. G. Hadjimitsis. Low-level mixing height detection in coastal locations with a scanning Doppler lidar. *Atmospheric Measurement Techniques*, 8(4):1875–1885, 2015. doi: 10.5194/amt-8-1875-2015.

T. Vesala, L. Järvi, S. Launiainen, A. Sogachev, Ü. Rannik, I. Mammarella, E. Siivola, P. Keronen, J. Rinne, A. Riikonen, and E. Nikinmaa. Surfaceatmosphere interactions

over complex urban terrain in Helsinki, Finland. *Tellus B*, 60(2):188–199, 2008. ISSN 1600-0889. doi: 10.1111/j.1600-0889.2007.00312.x.

U. Wandinger. *Introduction to Lidar*, pages 1–18. Springer New York, New York, NY, 2005. ISBN 978-0-387-25101-1. doi: 10.1007/0-387-25101-4_1.

J. M. White, J. F. Bowers, S. R. Hanna, and J. K. Lundquist. Importance of using observations of mixing depths in order to avoid large prediction errors by a transport and dispersion model. *Journal of Atmospheric and Oceanic Technology*, 26(1):22–32, 2009. doi: 10.1175/2008JTECHA1134.1.

C. R. Wood, A. Lacser, J. F. Barlow, A. Padhra, S. E. Belcher, E. Nemitz, C. Helfter, D. Famulari, and C. S. B. Grimmond. Turbulent flow at 190 m height above London during 2006–2008: A climatology and the applicability of similarity theory. *Boundary-Layer Meteorology*, 137(1):77–96, 2010. ISSN 1573-1472. doi: 10.1007/s10546-010-9516-x.

R. Wood. Stratocumulus clouds. *Monthly Weather Review*, 140(8):2373–2423, 2012. doi: 10.1175/MWR-D-11-00121.1.